APP fragment controls both ionotropic and non-ionotropic signaling of NMDA receptors

Jade Dunot, Sebastien Moreno, Carine Gandin, Paula A Pousinha, Mascia Amici, Julien Dupuis, Margarita Anisimova, Alex Winschel, Magalie Uriot, Samuel J Petshow, et al.

▶ **To cite this version:**

Jade Dunot, Sebastien Moreno, Carine Gandin, Paula A Pousinha, Mascia Amici, et al.. APP fragment controls both ionotropic and non-ionotropic signaling of NMDA receptors. Neuron, 2024, 112 (16), pp.2708-2720.e9. 10.1016/j.neuron.2024.05.027 . hal-04742865

HAL Id: hal-04742865

https://hal.science/hal-04742865v1

Submitted on 18 Oct 2024

Neuron

Report

APP fragment controls both ionotropic and non-ionotropic signaling of NMDA receptors

Highlights

- AETA hampers NMDA receptor ionotropic activity by competing with its co-agonists
- AETA modifies NMDA receptor conformation and enhances ion-flux-independent signaling
- AETA level is raised by increased neuronal activity
- Deletion of AETA modifies NMDA receptor signaling and associated synapse plasticity

Authors

Jade Dunot, Sebastien Moreno,
Carine Gandin, ..., Laurent Groc,
Michael Willem, Hélène Marie

Correspondence

mwillem@med.uni-muenchen.de (M.W.),
marie@ipmc.cnrs.fr (H.M.)

In brief

Dunot et al. identify AETA, a bioactive cleavage product of amyloid-β precursor protein, as a novel endogenous NMDA receptor regulator. AETA competes with receptor co-agonists, thereby modulating ionotropic and non-ionotropic receptor activities. Chronic AETA loss impairs synaptic plasticity and memory. These findings highlight a new mechanism regulating brain information processing.

Dunot et al., 2024, Neuron *112*, 1–13
August 21, 2024
https://doi.org/10.1016/j.neuron.2024.05.027

CellPress

Please cite this article in press as: Dunot et al., APP fragment controls both ionotropic and non-ionotropic signaling of NMDA receptors, Neuron (2024), https://doi.org/10.1016/j.neuron.2024.05.027

Neuron

CellPress
OPEN ACCESS

Report

APP fragment controls both ionotropic and non-ionotropic signaling of NMDA receptors

Jade Dunot,[1,2,11] Sebastien Moreno,[1,11] Carine Gandin,[1] Paula A. Pousinha,[1] Mascia Amici,[3] Julien Dupuis,[4] Margarita Anisimova,[5] Alex Winschel,[6] Magalie Uriot,[4] Samuel J. Petshow,[5] Maria Mensch,[1] Ingrid Bethus,[1] Camilla Giudici,[7] Heike Hampel,[8] Benedikt Wefers,[7,9] Wolfgang Wurst,[2,7,9] Ronald Naumann,[10] Michael C. Ashby,[3] Bodo Laube,[6] Karen Zito,[5] Jack R. Mellor,[3] Laurent Groc,[4] Michael Willem,[8,*] and Hélène Marie[1,12,*]

[1]Université Côte d'Azur, CNRS, INSERM, Institut de Pharmacologie Moléculaire et Cellulaire, 06560 Valbonne, France
[2]Munich Cluster for Systems Neurology (SyNergy), 81377 Munich, Germany
[3]Centre for Synaptic Plasticity, School of Physiology, Pharmacology and Neuroscience, University of Bristol, Bristol BS8 1TD, UK
[4]Université de Bordeaux, CNRS, Interdisciplinary Institute for Neuroscience, 33076 Bordeaux Cedex, France
[5]Center for Neuroscience, University of California, Davis, Davis, CA 95618, USA
[6]Department of Biology, Neurophysiology und Neurosensory Systems, TU Darmstadt, 64287 Darmstadt, Germany
[7]German Center for Neurodegenerative Diseases (DZNE) Munich, 81377 Munich, Germany
[8]Biomedical Center (BMC), Division of Metabolic Biochemistry, Faculty of Medicine, Ludwig-Maximilians-Universität München, 81377 Munich, Germany
[9]Institute of Developmental Genetics, Helmholtz Zentrum München, 85764 Neuherberg, Germany
[10]Max Planck Institute of Molecular Cell Biology and Genetics, 01307 Dresden, Germany
[11]These authors contributed equally
[12]Lead contact
*Correspondence: mwillem@med.uni-muenchen.de (M.W.), marie@ipmc.cnrs.fr (H.M.)
https://doi.org/10.1016/j.neuron.2024.05.027

SUMMARY

NMDA receptors (NMDARs) are ionotropic receptors crucial for brain information processing. Yet, evidence also supports an ion-flux-independent signaling mode mediating synaptic long-term depression (LTD) and spine shrinkage. Here, we identify AETA (Aη), an amyloid-β precursor protein (APP) cleavage product, as an NMDAR modulator with the unique dual regulatory capacity to impact both signaling modes. AETA inhibits ionotropic NMDAR activity by competing with the co-agonist and induces an intracellular conformational modification of GluN1 subunits. This favors non-ionotropic NMDAR signaling leading to enhanced LTD and favors spine shrinkage. Endogenously, AETA production is increased by *in vivo* chemogenetically induced neuronal activity. Genetic deletion of AETA production alters NMDAR transmission and prevents LTD, phenotypes rescued by acute exogenous AETA application. This genetic deletion also impairs contextual fear memory. Our findings demonstrate AETA-dependent NMDAR activation (ADNA), characterizing AETA as a unique type of endogenous NMDAR modulator that exerts bidirectional control over NMDAR signaling and associated information processing.

INTRODUCTION

The *N*-methyl-D-aspartate receptor (NMDAR) is a critical glutamate-gated ion channel that plays a fundamental role in various brain functions, particularly in regulating synaptic strength through processes like long-term potentiation (LTP) and long-term depression (LTD), which are essential for memory formation.[1,2] Co-agonist binding of glycine or D-serine, in addition to glutamate, is required for the ionotropic activity of NMDARs.[3] While the ion channel function is well established,[3,4] an unconventional ion-flux-independent signaling mode of NMDARs promoting synapse depression and spine shrinkage has been described,[1,5–13] although this evidence has been challenged.[14] Notably, this unconventional NMDAR function is characterized by glutamate binding in the absence of co-agonist binding.[9,12] How this mode of NMDAR activity is controlled endogenously remains unknown. Here, we identified AETA (Aη) as a molecular key that controls both ionotropic and ion-flux-independent NMDAR signaling. AETA is a recently discovered peptide derived from amyloid-β precursor protein (APP) cleavage, with potential bioactivity at excitatory synapses.[15,16] Following the shedding of the APP ectodomain by η-secretase and subsequent cleavage by α- or β-secretases, long and short forms of AETA are generated (Aη-α and Aη-β, respectively) (Figure 1A) and subsequently secreted into the interstitial space.[16] Our findings demonstrate that AETA competes with the co-agonists of NMDARs and modifies the conformation of the GluN1 intracellular tails. AETA holds a unique capacity to impact both NMDAR functions, as it inhibits NMDAR ionotropic activity and associated calcium entry while favoring ion-flux-independent

Please cite this article in press as: Dunot et al., APP fragment controls both ionotropic and non-ionotropic signaling of NMDA receptors, Neuron (2024), https://doi.org/10.1016/j.neuron.2024.05.027

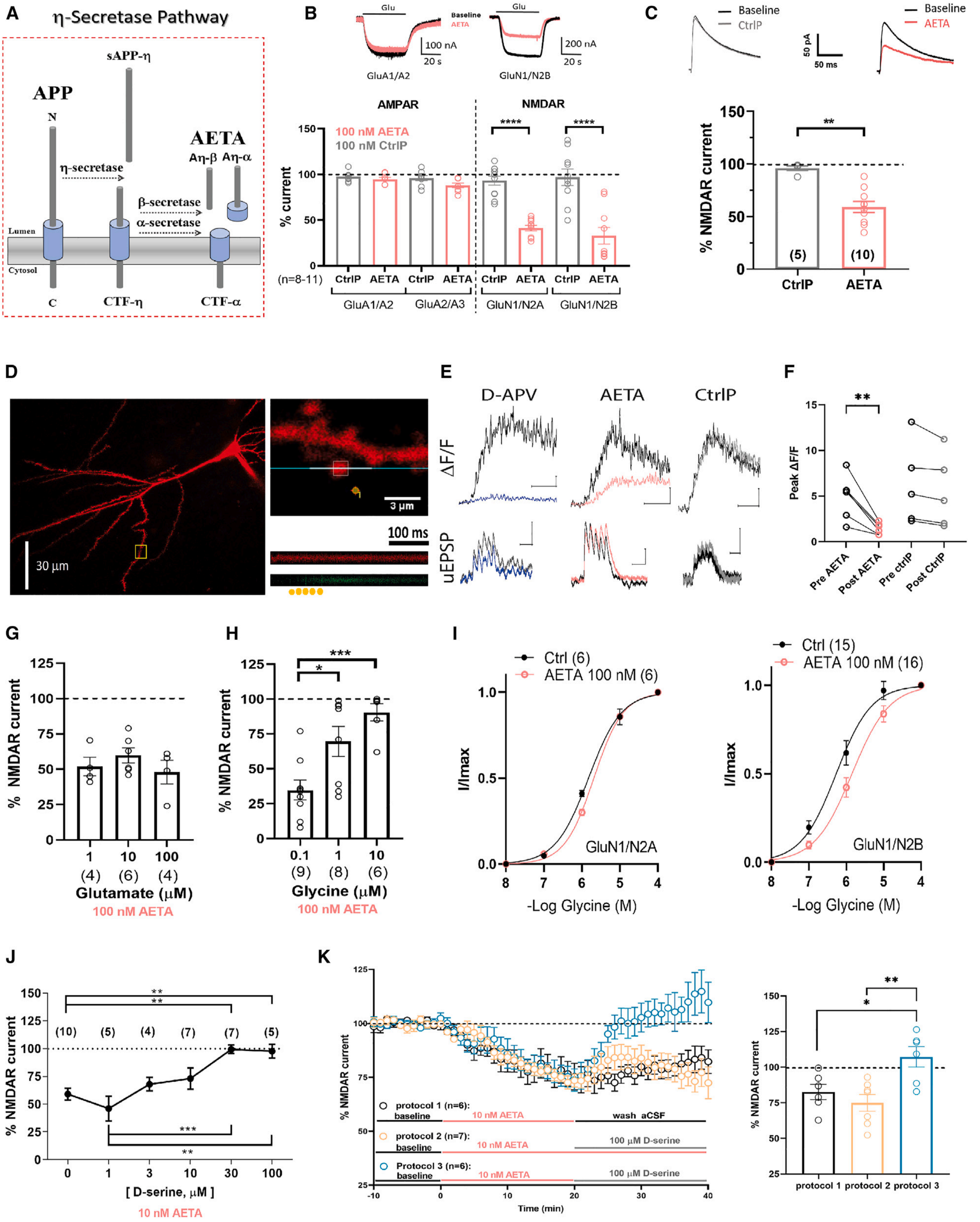

(legend on next page)

Please cite this article in press as: Dunot et al., APP fragment controls both ionotropic and non-ionotropic signaling of NMDA receptors, Neuron (2024), https://doi.org/10.1016/j.neuron.2024.05.027

synapse weakening and spine shrinkage. Furthermore, we provide evidence that AETA production is activity-dependent and essential for proper NMDAR transmission, LTD, and memory processing. Thus, our study unveils a novel endogenous modulator of NMDARs, shedding light on its crucial role in brain signaling.

RESULTS

AETA inhibits NMDAR ionotropic activity

Upon the discovery of AETA and its ability to reduce hippocampal LTP,[15,16] a process of synaptic potentiation that depends on NMDARs for induction and AMPA receptors (AMPARs) for expression, we first asked if AETA could directly modulate the activity of these glutamatergic receptors. We expressed recombinant forms of NMDARs (specifically GluN1/GluN2A or GluN1/GluN2B subtypes) or AMPARs (GluA1/GluA2 or GluA2/GluA3 subtypes) in *Xenopus* oocytes. We investigated the acute effects of AETA (100 nM) or a control peptide (CtrlP) (100 nM) on the current amplitudes of AMPARs and NMDARs. While AMPAR currents remained unaltered in the presence of AETA, there was a significant inhibition of NMDAR currents (Figure 1B). To further characterize this effect, we conducted a dose-response curve to determine the impact of varying concentrations of AETA on NMDAR currents. The results revealed a dose-dependent reduction in NMDAR current, allowing us to calculate the half-maximal inhibitory concentration (IC50) values for both receptor subtypes (1.62 nM for GluN1/N2A; 15.45 nM for GluN1/N2B) (Figure S1A). These findings confirm the direct modulatory action of AETA on NMDARs. Next, we evaluated the influence of AETA on native NMDAR in cultured neurons and in hippocampal slices. We previously reported bioactivity of AETA within a low nanomolar concentration range (5–10 nM).[15] To ensure the specificity of our findings and avoid any potential nonspecific effects, we conducted all subsequent analyses on native receptors using a concentration of 10 nM AETA. Notably, this concentration also inhibited recombinant GluN1/N2B NMDARs in oocytes (62.98 ± 8.28%; normalized to averaged baseline; data not shown). In cultured neurons, application of NMDA puffs resulted in currents that remained unchanged after a 10-min incubation with CtrlP (Figure S2A). By contrast, the presence of AETA led to a progressive decrease in current amplitude, which eventually reached a plateau at 55% of the original amplitude (Figure S2A). Similarly, in hippocampal slices from young adult mice, native synaptic NMDAR currents recorded at the CA3–CA1 synapse (comprising approximately 80% GluN1/N2A and 20% GluN1/N2B subtypes[17]) were reduced by AETA reaching a plateau at 65% of the original amplitude, while no change was observed with CtrlP (Figures 1C and S2B). Using pharmacological blockage of GluN2A- or GluN2B-containing NMDARs with TCN-201 or ifenprodil, respectively, we observed that AETA's effect was stronger on native GluN2A-containing than on GluN2B-containing NMDARs (Figure S2C). Conversely, native synaptic AMPAR currents measured in hippocampal slices remained unaffected by AETA (Figure S3A). In addition, spontaneous excitatory postsynaptic currents (sEPSCs) mediated by NMDARs were also impacted by AETA but not by CtrlP, leading to a decrease in NMDAR sEPSC frequency (Figures S4 and S5). Again, sEPSCs mediated by AMPARs showed no significant alterations (Figures S3B–E and S5). The paired-pulse ratio (PPR), which serves as a measure of presynaptic short-term plasticity, remained unaltered (Figure S3F), providing evidence against any

Figure 1. AETA inhibits NMDA receptor ionotropic activity

(A) Depicted is the η-secretase-dependent processing of APP. Shedding occurs within the luminal ectodomain, liberating sAPP-η, while the membrane-bound C-terminal fragment (CTF-η) is further processed alternatively by either α- or β-secretases releasing longer or shorter forms of AETA, respectively (Aη-α and Aη-β).

(B) (Top) Representative current traces quantified in oocytes expressing recombinant AMPARs containing GluA1/GluA2 (left) or NMDARs containing GluN1/GluN2B (right) before (black) and after (red) application of AETA (100 nM). NMDAR recordings were made in the presence of 100 μM L-glutamate/1 μM glycine. AMPAR recordings were made in the presence of L-glutamate (300 μM) and cyclothiazide (CTZ) (100 μM). (Bottom) Graph represents % peak current (normalized to averaged baseline) of AMPARs (either GluA1/GluA2 or GluA2/GluA3) and NMDARs (either GluN1/GluN2A or GluN1/GluN2B) after application of either AETA (100 nM) or control peptide (CtrlP) (100 nM). *n* = between 8 and 11 independent oocytes per condition.

(C) (Top) Representative traces of NMDAR currents recorded at CA3–CA1 synapses of adult mouse slices before (baseline, black) and after application of CtrlP (10 nM, gray) or AETA (10 nM, red). (Bottom) Bar graph of AETA or CtrlP effect on NMDAR EPSC calculated 25–30 min post application (full time course shown in Figure S2B). *n* = number of patched neurons per condition.

(D) Two-photon image of CA1 hippocampal neuron filled with Alexa 594 (red) and Fluo-5F (green). Boxed area is enlarged on right with uncaging spot indicated in yellow and line scan indicated in white. Dual channel line scan images with response to five uncaging events (50 Hz, yellow dots) shown below.

(E) Line scan profiles across spine heads (scale bars: 100 ms/$\Delta F/F$ 2 a.u.) and simultaneous electrophysiological recordings of uEPSP (scale bars: 50 ms/0.5 mV) in response to five uncaging events before (black) and after D-APV (100 μM, blue), AETA (10 nM, red), or CtrlP (10 nM, gray).

(F) Peak spine calcium transients are depressed after 10 min of 10 nM AETA application (*n* = 6 neurons) but not after CtrlP application (*n* = 5).

(G and H) Effect of AETA (100 nM) on NMDAR current in oocytes expressing GluN1/GluN2B in the presence of different concentrations of glutamate (1; 10 or 100 μM) (G) or glycine (0,1; 1 or 10 μM) (H). *n* = oocytes per condition.

(I) Dose-response activation curves for glycine in absence or presence of AETA (100 nM) measured in oocytes expressing either GluN1/GluN2A (left) or GluN1/GluN2B (right).

(J) Dose-response curve of AETA's effect (10 nM) on native NMDAR current at CA3–CA1 synapses in mouse hippocampal slices measured by patch clamp in the presence of different concentrations of D-serine (0, 1, 3, 10, 30, and 100 μM) in recording solution. *n* = neurons patched per condition.

(K) (Left) Time course of AETA's effect (10 nM) on NMDAR currents at CA3–CA1 synapses in mouse hippocampal slices measured during different washout protocols. Protocol 1, 20 min AETA (10 nM) followed by washout with aCSF; protocol 2, 20 min AETA (10 nM) followed by addition of D-serine (100 μM) but in continuous presence of AETA; protocol 3, 20 min AETA (10 nM) followed by substitution with D-serine (100 μM). (Right) Time course data plotted as a bar graph showing % NMDAR current measured during last 5 min for each protocol (normalized to averaged baseline current of that protocol).

Error bars represent standard error of the mean (s.e.m.); * $p < 0.05$; ** $p < 0.01$; *** $p < 0.001$; **** $p < 0.0001$. Statistics: One-way ANOVA followed by Tukey's multiple comparisons test (B, G, H, J, and K); Mann-Whitney test (C); Paired Student's t test (F). See supplemental statistics (Data S1) for full statistics. See also Figures S1–S5 for additional experiments related to Figure 1.

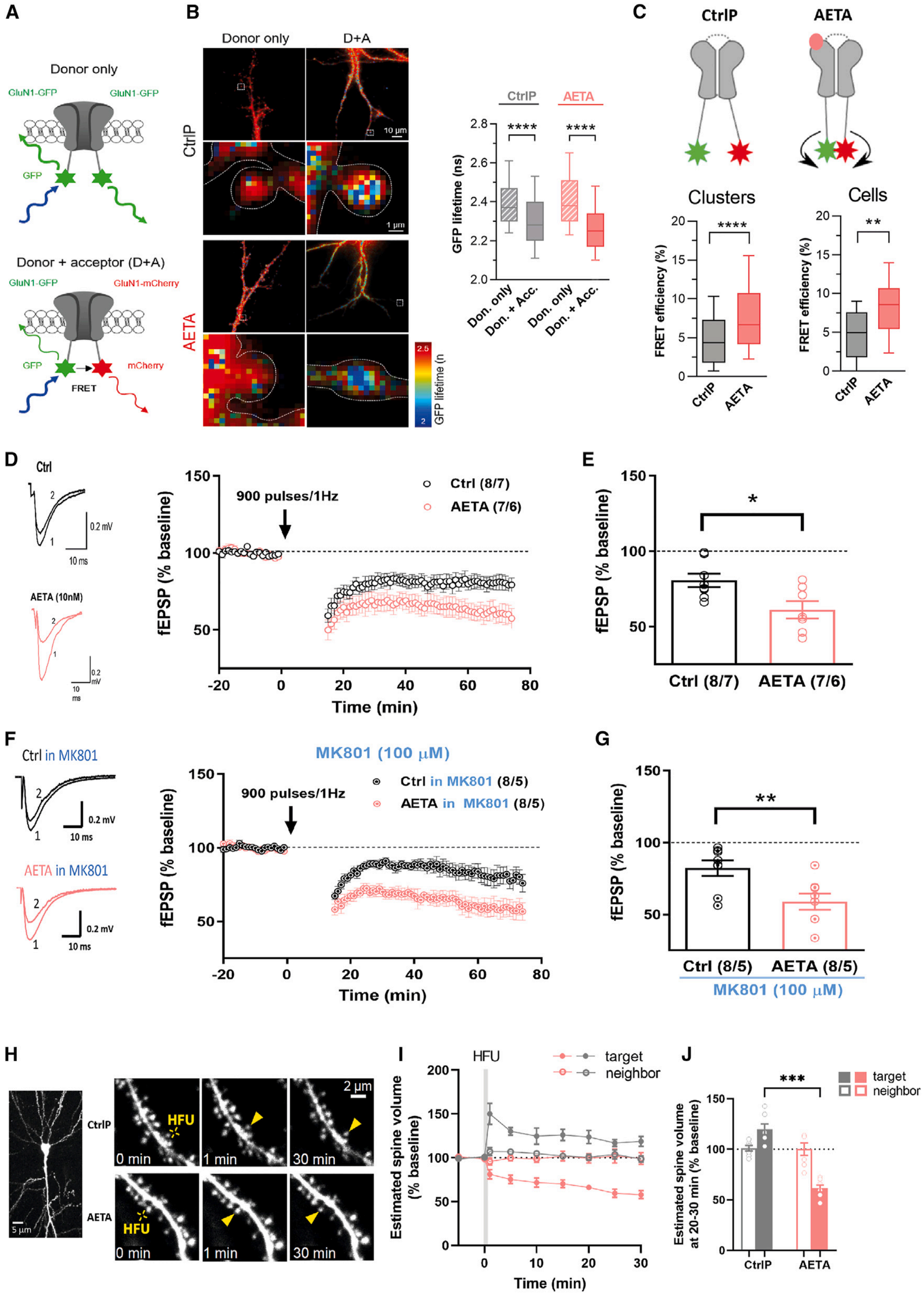

(legend on next page)

Please cite this article in press as: Dunot et al., APP fragment controls both ionotropic and non-ionotropic signaling of NMDA receptors, Neuron (2024), https://doi.org/10.1016/j.neuron.2024.05.027

presynaptic effect of AETA on release probability. Collectively, the data, obtained from three distinct analysis systems, consistently support the conclusion that AETA acts directly and acutely at the postsynaptic site, specifically inhibiting NMDAR transmission while not affecting AMPAR transmission.

Given AETA's ability to inhibit NMDAR current, it is expected that it would also reduce NMDAR-dependent calcium entry into dendritic spines, thereby preventing NMDAR ionotropic signaling. To investigate this, we employed two-photon single-spine calcium imaging in conjunction with glutamate uncaging to evoke unitary excitatory postsynaptic potential (uEPSP) recorded at CA3–CA1 synapses in hippocampal slices. By monitoring the activity of individual spines upon glutamate uncaging (Figures 1D and 1E), we confirmed that AETA, but not CtrlP, significantly attenuated NMDAR-dependent calcium entry (Figure 1F) without attenuating EPSP amplitude or changing the resting membrane potential (data not shown). These findings provide further evidence that AETA effectively inhibits NMDAR ionotropic signaling by impeding calcium influx in the presence of glutamate stimulation.

AETA competes with NMDAR co-agonist to inhibit ionotropic activity

The activation of NMDARs involves complex conformational rearrangements across extracellular, transmembrane, and cytosolic receptor domains, requiring the binding of glutamate and glycine/D-serine as co-agonists.[3,4] To investigate the mechanism of AETA's inhibitory activity, we conducted experiments using oocytes to assess its dependence on the concentration of these two ligands. Modulating the levels of glutamate in the recording bath prior to AETA application did not alter its effect (Figure 1G), indicating that glutamate availability did not influence AETA's inhibitory action. However, increasing the levels of glycine significantly diminished the impact of AETA (Figure 1H). These findings suggest that AETA competes with the co-agonist at the glycine/D-serine binding site. To further validate this hypothesis, we performed dose-response curves for glycine in the absence and presence of AETA on both GluN1/GluN2A and GluN1/GluN2B NMDAR receptor subtypes. AETA shifted these curves to the right and increased the half-maximal effective concentration (EC50) for glycine (Figures 1I, S1B, and S1C), indicating a competitive binding of AETA at the co-agonist site. To confirm the competitive action of AETA on native synaptic NMDARs, we investigated its effect on isolated NMDAR currents of CA3–CA1 synapses in hippocampal slices at varying concentrations of D-serine. We used D-serine instead of glycine when recording NMDAR currents in CA1 neurons because D-serine is the primary co-agonist for native synaptic NMDA receptors.[18] Increasing the dose of D-serine in the recording bath progressively attenuated the effect of AETA, completely blocking it at 30–100 μM (Figure 1J). We also examined the duration of AETA's effect after the removal of the peptide and its susceptibility to competition by D-serine (Figure 1K). The inhibition of NMDAR current by AETA persisted for at least 20 min after its removal, suggesting that AETA binds to and modifies NMDAR activity in a lasting manner. Moreover, the addition of D-serine (100 μM) to AETA did not relieve the inhibition of NMDARs, indicating that AETA binds to NMDARs with higher affinity than D-serine. Conversely, replacing AETA with D-serine restored NMDAR activity, confirming the competitive nature of AETA's interaction with the co-agonist.

AETA alters NMDAR conformation

Previous studies showed that agonist and co-agonist binding induce conformational changes in the cytosolic domains of NMDARs, affecting both ionotropic and non-ionotropic signaling pathways.[7,19] Given the role of AETA as a potential endogenous regulator of NMDAR co-agonist binding, we investigated whether AETA elicits similar conformational rearrangements. To explore this, we utilized fluorescence lifetime imaging

Figure 2. AETA modifies NMDAR conformation, enhances LTD via non-ionotropic activity of NMDARs, and promotes spine shrinkage

(A) Schematic principle of intramolecular FLIM-FRET experiment. Hippocampal neurons were transfected either with GluN1-GFP alone (donor only, upper panel) or in combination with GluN1-mCherry (donor + acceptor, lower panel; all constructs co-transfected with GluN2B-flag). Upon excitation of the GFP fluorophore with blue light, the proximity of GluN1-GFP and GluN1-mCherry within a receptor and overlap of GFP emission and mCherry excitation spectra allow resonance energy transfer (black arrow) from the donor fluorophore (GFP) to the acceptor fluorophore (mCherry), causing excitation of the acceptor fluorophore (red arrow) and a subsequent decrease in the fluorescence lifetime of the donor fluorophore (green arrows).

(B) Representative illustrations of GFP lifetime in neuronal fields (upper panels) and GluN1-GFP only (donor only) and GluN1-GFP/GluN1-mCherry (D + A) dendritic spine clusters (lower panels) 10 min after exposure to CtrlP or AETA (10 nM). Graph represents GFP lifetime in GluN1-GFP only (Don. only) and GluN1-GFP/GluN1-mCherry (Don. + Acc.) clusters 10 min after exposure to CtrlP (10 nM; Don. only, n = 738 clusters; Don. + Acc., n = 432 clusters) or AETA (10 nM; Don. only, n = 796 clusters; Don. + Acc., n = 299 clusters).

(C) (Left) FRET efficiency in GluN1-GFP/GluN1-mCherry clusters 10 min after exposure to CtrlP (10 nM; n = 432 clusters) or AETA (10 nM; n = 299 clusters). (Right) FRET efficiency in GluN1-GFP/GluN1-mCherry clusters averaged per cell 10 min after exposure to CtrlP (10 nM; n = 23 cells) or AETA (10 nM; n = 18 cells). (Top) Diagram of movement of GluN1 intracellular tail in control condition (CtrlP) and in the presence of AETA.

(D) Representative traces (left, 1 shows trace pre- and 2 shows trace post-induction) and summary graph (right) of fEPSP slope (% baseline) pre- and post-LTD induction (time 0) in control (Ctrl, aCSF only) or in the presence of AETA (10nM) throughout recording.

(E) Summary of fEPSP magnitude 45–60 min after LTD induction as fEPSP (% baseline) for data shown in (D). n/N = number of slices/mice.

(F–G) same as in (D–E) but in the presence of 100 μM MK801 (3 h pre-incubation and throughout recording).

(H) (Left) Low-magnification image of GFP-labeled CA1 pyramidal neuron from P18-21 GFP-M mice. (Right) High-magnification images of basal dendrites of CA1 pyramidal neurons from GFP-M mice before (time 0) and after (1 and 30 min) high-frequency glutamate uncaging (HFU, yellow cross) at an individual dendritic spine (yellow arrowhead) in the presence of 10 nM CtrlP or AETA.

(I–J) HFU-induced spine growth in the presence of CtrlP (gray filled circles/bar; n/N = 7 cells/6 mice) was converted to spine shrinkage in the presence of AETA (red filled circles/bar; n/N = 7 cells/6 mice). The volume of unstimulated neighboring spines (open circles/bars) was unchanged.

Error bars represent s.e.m.; * $p < 0.05$; ** $p < 0.01$; *** $p < 0.001$; **** $p < 0.0001$. Statistics: Kruskal-Wallis test followed by Dunn's multiple comparisons test (B); Mann-Whitney test (C); unpaired Student's t test (E and G); two-way ANOVA with Bonferroni's multiple comparisons test (J). See supplemental statistics (Data S1) for full statistics. See also Figures S6 and S7 for additional experiments related to Figure 2.

Please cite this article in press as: Dunot et al., APP fragment controls both ionotropic and non-ionotropic signaling of NMDA receptors, Neuron (2024), https://doi.org/10.1016/j.neuron.2024.05.027

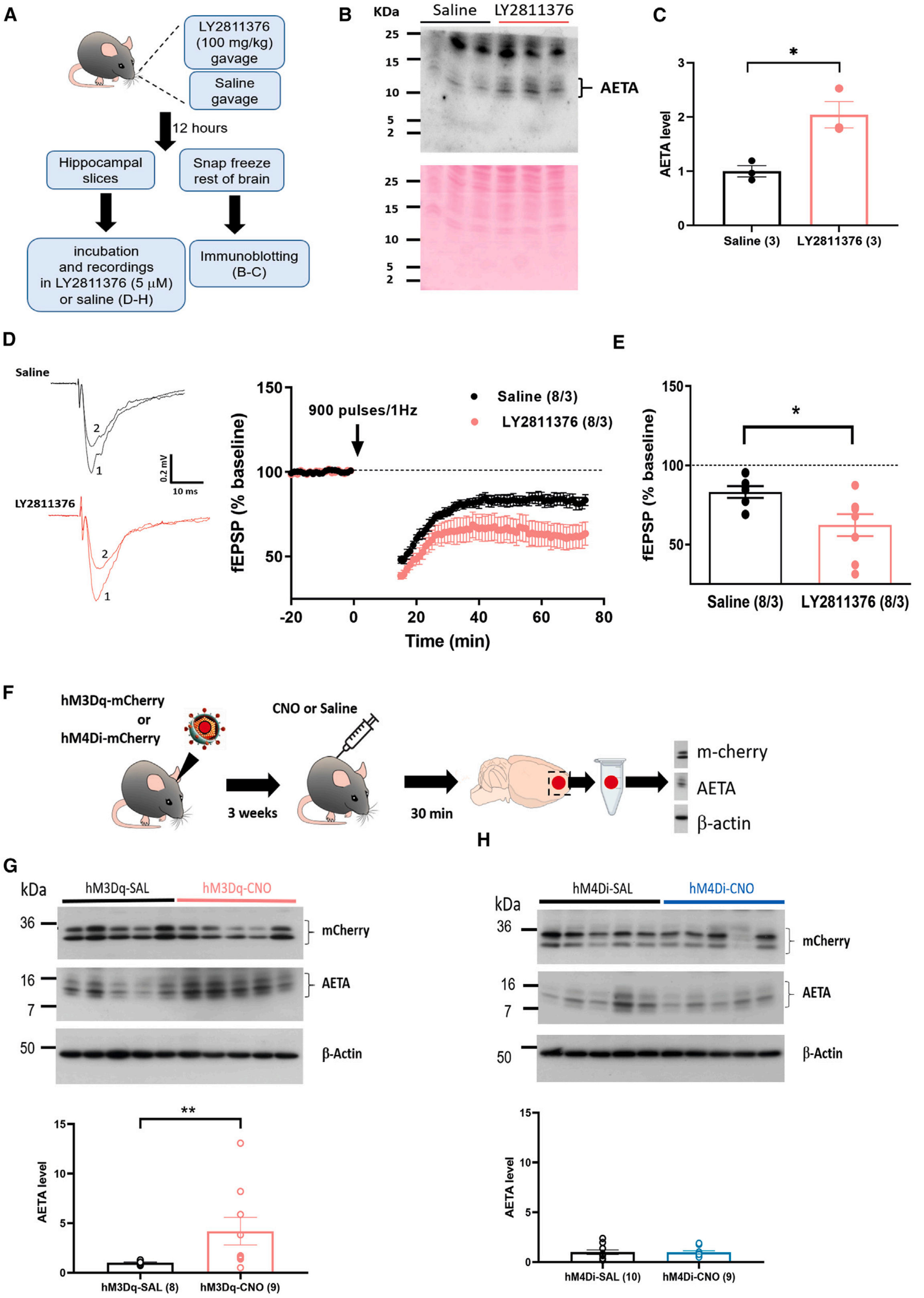

(legend on next page)

Please cite this article in press as: Dunot et al., APP fragment controls both ionotropic and non-ionotropic signaling of NMDA receptors, Neuron (2024), https://doi.org/10.1016/j.neuron.2024.05.027

microscopy (FLIM) in hippocampal neurons expressing recombinant GluN1-NMDAR subunits. Förster resonance energy transfer (FRET) was measured between C-terminal domains labeled with green fluorescent protein (GFP) or mCherry fluorophores as an indicator of intracellular conformational changes (Figures 2A and 2B).[7,19] As expected, the lifetime decreased between the "donor only" and "donor/acceptor" conditions in the presence of CtrlP or AETA peptides (Figure 2B, graph). Exposure to CtrlP for 10 min resulted in fluorescence lifetime values comparable to those reported in buffer,[19] indicating no significant effect on conformational changes (Figure 2C). In contrast, AETA exposure for the same duration induced a substantial increase in FRET efficiency (Figure 2C). This conformational change is independent of agonist binding, as AETA equally increases FRET efficiency in the presence of the NMDAR antagonist APV (50 μM) (Figures S6A and S6B). These findings demonstrate that, similarly to co-agonists, AETA binding triggers conformational rearrangements in the C-terminal domains of GluN1, bringing them into closer proximity in a receptor-activity-independent manner (Figure 2C, diagram). These rearrangements putatively modulate associated cytosolic protein complexes and signaling pathways. There is evidence that activation of the p38 kinase via its phosphorylation represents a downstream signaling pathway of NMDARs, notably in the context of ion-flux-independent signaling.[9,13,20] In line with these data, we found that AETA increased p38 phosphorylation in cultured neurons (Figures S6C and S6D). This suggests that AETA might favor NMDAR ion-flux-independent signaling.

AETA enhances LTD via non-ionotropic activity of NMDARs and promotes spine shrinkage

The reduced ionotropic signaling of NMDARs, which includes decreased calcium entry, is consistent with the impairment of LTP caused by AETA.[15,16] However, it is important to consider that a decrease in NMDAR-dependent calcium signaling could also affect LTD, as sustained low levels of NMDAR-dependent calcium entry have been shown to induce LTD.[2] Alternatively, the altered conformation of NMDARs caused by AETA and increase in p38 phosphorylation may promote non-ionotropic NMDAR signaling, which has been reported to also play a critical role in LTD.[7,9,12,20,21] We thus examined the impact of AETA on LTD at the CA3–CA1 synapse in hippocampal slices (Figures 2D and 2E). We found that AETA enhanced the magnitude of LTD induced by 900 stimuli at 1 Hz. Additionally, even with a subthreshold LTD induction protocol of 300 stimuli at 1 Hz that did not induce LTD in control conditions, the presence of AETA still resulted in the production of LTD (Figures S7A and S7B). These findings demonstrate that AETA favors LTD, potentially through its influence on NMDAR conformation and non-ionotropic signaling pathways rather than solely through alterations in calcium signaling. Despite some controversy,[8–11,14] evidence suggests that LTD can be mediated by NMDAR activity without requiring ion flux, as demonstrated by the occurrence of LTD in the presence of the ion channel blocker MK801.[9] To validate this, we replicated the conditions reported previously[9] and observed LTD at CA3–CA1 synapses in rat hippocampal slices in the presence of MK801 (Figures S7C and S7D). Next, we examined whether enhanced LTD mediated by AETA could still occur in the presence of MK801. In mouse slices, we preincubated the slices with MK801 for 3 h, confirming that this application of MK801 completely blocked the ionotropic function of NMDARs as expected (Figure S7E). Notably, also in mouse slices, we observed LTD in the presence of MK801 (Figures 2F and 2G). AETA still enhanced this ion-flux-independent LTD (Figures 2F and 2G). These data provide evidence that AETA binding promotes ion-flux-independent NMDAR activity, which mediates LTD.

Synaptic plasticity at excitatory glutamatergic synapses is closely linked to structural changes in dendritic spines, wherein synaptic weakening is accompanied by spine shrinkage.[22,23] Previous studies have provided evidence that glutamate binding to NMDARs in the absence of ion flux is sufficient to mediate LTD-induced spine shrinkage,[12,20] and p38 activity is involved in this phenomenon.[13,20] Moreover, a decrease in co-agonist levels has been shown to bias spine structural plasticity toward shrinkage.[24] Given AETA's ability to compete with co-agonist binding and to increase p38 phosphorylation, we hypothesized that AETA could promote spine shrinkage. To test this hypothesis, we employed a high-frequency glutamate uncaging (HFU) protocol typically associated with spine growth at single

Figure 3. Endogenous increase of AETA by *in vivo* BACE1 inhibition leads to increased LTD, and endogenous AETA production increases with *in vivo* neuronal activity

(A) Diagram of experimental plan. The BACE1 inhibitor LY2811376 (or saline) was administered by gavage 12 h before sacrificing the mouse. Brains were removed to prepare hippocampal slices for electrophysiology (D–E). The rest of the brains were used for immunoblotting to check for increase in AETA (B–C).

(B) Ponceau staining and immunoblot (M3.2 antibody) of AETA from saline- and LY2811376-treated brains.

(C) Quantification of levels of AETA in saline- and LY2811376-treated brains (normalized to Ponceau). *N* = number of mice.

(D) Representative traces (left, 1 shows trace pre- and 2 shows trace post-induction; scale bars: 10 ms/0.2 mV) and summary graph (right) of fEPSP slope (% baseline) pre- and post-LTD induction (time 0) at CA3–CA1 synapses in hippocampal slices from saline- and LY2811376-treated mice.

(E) Bar graph of fEPSP magnitude 45–60 min after LTD induction as fEPSP (% baseline) for data shown in (D). *n*/*N* = slices/mice.

(F) Diagram of experimental design to activate or inhibit neurons *in vivo* using AAV-hM3Dq-mCherry or AAV-hM4Di-mCherry, respectively, and quantify AETA levels.

(G) (Top) Example of immunoblot showing detection of mCherry, AETA, and β-actin in hM3Dq-transduced tissue after saline or CNO i.p. injection. (Bottom) Quantification of AETA in hM3Dq-SAL and hM3Dq-CNO (normalized to β-actin and mCherry). All quantified blots are provided in Figures S9C and S9D. *N* = number of mice.

(H) (Top) Example of immunoblot showing detection of mCherry, AETA, and β-actin in hM4Di-transduced tissue after saline or CNO i.p. injection. (Bottom) Quantification of AETA in hM4Di-SAL and hM4Di-CNO (normalized to β-actin and mCherry). All quantified blots are provided in Figures S9E and S9F. *N* = number of mice.

Error bars represent s.e.m.; $^{*}p < 0.05$; $^{**}p < 0.01$. Statistics: unpaired Student's t test (C and E); Mann-Whitney test (G and H). See supplemental statistics (Data S1) for full statistics. See also Figures S8 and S9 for additional experiments related to Figure 3.

Please cite this article in press as: Dunot et al., APP fragment controls both ionotropic and non-ionotropic signaling of NMDA receptors, Neuron (2024), https://doi.org/10.1016/j.neuron.2024.05.027

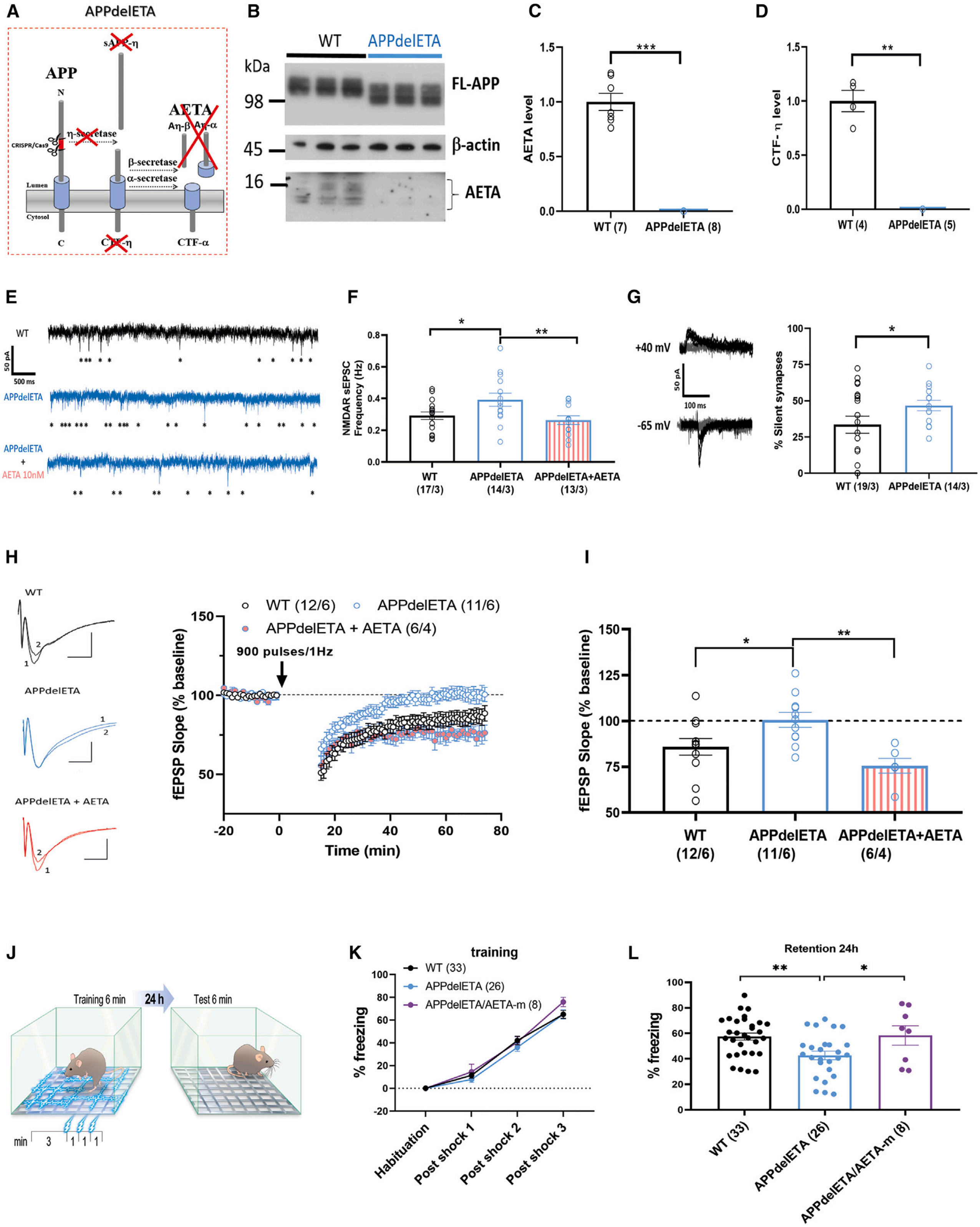

(legend on next page)

Please cite this article in press as: Dunot et al., APP fragment controls both ionotropic and non-ionotropic signaling of NMDA receptors, Neuron (2024), https://doi.org/10.1016/j.neuron.2024.05.027

dendritic spines on basal dendrites of CA1 hippocampal neurons in acute slices from GFP-M mice, where GFP is selectively expressed in a subset of hippocampal pyramidal neurons (Figure 2H).[24] As expected, the HFU protocol led to dendritic spine growth in the presence of the CtrlP, whereas the presence of AETA instead induced spine shrinkage (Figures 2I and 2J). These results show shrinkage under conditions that would normally be expected to induce long-term spine growth, consistent with AETA's promoting non-ionotropic NMDAR signaling.

Increasing endogenous AETA levels with BACE1 inhibition decreases NMDAR activity and enhances LTD

The experiments described above rely on exogenous application of synthetic AETA. To provide stronger *in vivo* evidence for these findings, we asked if increasing endogenous AETA levels could also lead to alterations in NMDAR activity and synapse plasticity. There is no pharmacological compound that specifically targets AETA production. Yet, we previously reported that BACE1 inhibition leads to an increase in endogenous AETA.[16] We thus inhibited BACE1 *in vivo* with oral gavage of the BACE1 inhibitor LY2811376 (Figure 3A).[25] This indeed led to a 2-fold increase in endogenous AETA (Figures 3B and 3C). We prepared hippocampal slices from these mice and kept them in LY2811376 throughout the recordings. We observed that increased AETA correlated with decreased NMDAR sEPSC frequency, but not amplitude (Figure S8), and increased LTD (Figures 3D and 3E), thus reproducing exactly the phenotypes observed with acute application of synthetic AETA.

AETA production is enhanced by neuronal activity

We here demonstrated that AETA functions as a novel modulator of NMDARs. To further establish its classification as an endogenous neuromodulator, we investigated whether AETA levels can be regulated by neuronal activity, as is the case for known neuromodulators. We employed chemogenetic designer receptor exclusively activated by designer drugs (DREADD) proteins hM3Dq and hM4Di to manipulate neuronal activity *in vivo*. Neurons in the prefrontal cortex were transduced with an adeno-associated virus (AAV) expressing either hM3Dq or hM4Di along with mCherry (Figures 3F, and S9A, and S9B). After three weeks of expression, mice were injected with either saline (control) or clozapine *N*-oxide (CNO) to activate or inhibit the transduced neurons (Figure 3F). Thirty minutes after CNO injection, we microdissected the mCherry-labeled region of the prefrontal cortex and quantified AETA levels in these tissues using immunoblotting. Our results revealed a significant 4-fold increase in AETA levels in samples subjected to neuronal activation (Figures 3G, S9C, and S9D). By contrast, inhibition of neuronal activity did not alter AETA levels (Figures 3H, S9E, and S9F). Viral expression did not otherwise alter markers of synapse integrity (Figures S9G and S9H). Therefore, AETA production is specifically linked to an elevation in neuronal activity.

AETA is necessary for adequate NMDAR ionotropic activity, LTD, and memory processing

To further establish AETA as an activity-dependent regulator of NMDARs, we conducted experiments to determine its necessity for this signaling mechanism. Utilizing CRISPR-Cas9 gene editing, we generated a novel mouse model, termed the APPdelETA mouse, in which the η-secretase cleavage site of the endogenous APP was deleted (Figure 4A). This expectedly resulted in a smaller mutant APP (Figure 4B). Consequently, AETA and its membrane-bound precursor peptide CTF-η were absent in these mice (Figures 4B–D and S10A–C). Recording NMDAR-mediated sEPSCs in CA1 pyramidal neurons of the APPdelETA mice, we observed higher frequency (Figures 4E and 4F) but normal amplitude (Figure S10F) of these currents compared with control littermates. Importantly, we were able to normalize NMDAR sEPSC frequency by the acute exogenous application of AETA (Figures 4E and 4F). By contrast, neither AMPAR

Figure 4. APPdelETA mice display altered NMDAR transmission, loss of LTD, and reduced memory

(A) Depicted is the prevention of η-secretase-dependent processing of APP due to a 41-amino-acid in-frame deletion (marked in red; CRISPR/Cas9 gene editing) in the APPdelETA mouse model. Due to this deletion, no η-secretase shedding occurs (no sAPP-η), and the membrane-bound C-terminal fragment (CTF-η) and AETA peptides are not produced in homozygous APPdelETA mice.

(B) Example of an immunoblot of hippocampal tissue showing detection of full-length APP (FL-APP), β-actin (loading control), and AETA in WT and APPdelETA hippocampal lysates. Note that FL-APP is smaller in size in APPdelETA tissue due to endogenous deletion.

(C) Quantification of endogenous AETA levels in WT and APPdelETA hippocampi, normalized to β-actin levels. All quantified blots are provided in Figures S10A and S10B. *N* = number of mice.

(D) Quantification of endogenous CTF-η levels (precursor of AETA) in WT and APPdelETA hippocampi, normalized to β-actin levels. Quantified blot is provided in Figure S10C. *N* = number of mice.

(E) Representative traces of NMDAR sEPSCs recorded in CA1 pyramidal neurons of slices from WT mice and APPdelETA mice and in APPdelETA mice in the presence of AETA (10 nM) in the recording bath.

(F) NMDAR sEPSC frequency calculated from traces as shown in (E). *n*/*N* = neurons/mice.

(G) Traces show ten consecutive synaptic responses recorded at −65 mV and +40 mV evidencing responses (black) and failures (gray). Bar graph shows calculated percentage of silent synapses in WT and APPdelETA neurons. *n*/*N* = neurons/mice.

(H) Representative traces (left, 1 shows trace pre- and 2 shows trace post-induction; scale bars: 10 ms/0.2 mV) and summary graph (right) of fEPSP slope (% baseline) pre- and post-LTD induction (time 0) at CA3–CA1 synapses in hippocampal slices of WT and APPdelETA mice without or with supplementation of 10 nM AETA (in recording bath).

(I) Bar graph of fEPSP magnitude 45–60 min after LTD induction as fEPSP (% baseline) for data shown in (H). *n*/*N* = slices/mice.

(J) Diagram of contextual fear conditioning behavioral task.

(K) Graph represents % freezing measured during 6 min of training session in the three genotypes. *N* = number of mice.

(L) Graph represents % freezing measured during 6 min of test session done 24 h after training session.

Error bars represent s.e.m.; * $p < 0.05$; ** $p < 0.01$; ** $p < 0.001$. Statistics: Mann-Whitney test (C and D); one-way ANOVA followed by uncorrected Fisher's LSD test (F and L); unpaired Student's t test (G); one-way ANOVA followed by Tukey's multiple comparisons test (I); two-way ANOVA (K). See supplemental statistics (Data S1) for full statistics. See also Figures S10–S14 for additional experiments related to Figure 4.

sEPSCs (Figure S10D and S10E) nor the PPR (Figure S10G) showed alterations in these AETA-depleted neurons. Higher NMDAR sEPSC frequency in APPdelETA neurons could be due to an increase in NMDAR-only synapses (called silent synapses). Using a minimal stimulation protocol,[26] we quantified these silent synapses in wild-type (WT) and APPdelETA mice. We observed an increase in the percentage of silent synapses in APPdelETA mice (Figures 4G and S11). Yet, this alteration in the number of silent synapses was not correlated to an increase in the number of spines in these neurons as quantified by Golgi-Cox staining (Figure S12). Moreover, LTD could not be induced in hippocampal slices at CA3–CA1 synapses of adult APPdelETA mice, and this deficit was rescued by the acute exogenous application of AETA (Figures 4H and 4I). LTD could not be rescued by a competitive antagonist of the glycine/D-serine site (L689,560) (Figure S13), suggesting that AETA acts differently from these types of pharmacological compounds. By contrast, LTP was normal at these AETA-depleted synapses (Figures S10H and S10I). Finally, to assess the impact of loss of η-secretase-dependent processing of APP on NMDAR-dependent memory processes, we subjected these mice to contextual fear conditioning, a task known to rely on the hippocampus and NMDARs (Figure 4J). Notably, APPdelETA mice exhibited normal behavior during training but reduced freezing behavior 24 h after training compared with control littermates (Figures 4K and 4L). To rescue this deficit, we crossed APPdelETA mice with another mouse line, the AETA-m line, which harbors a transgene expressing a secreted form of human AETA in the brain (Figure S14). Re-expression of AETA normalized the memory phenotype (Figure 4L). Collectively, these data strongly support the notion that AETA is indispensable for proper hippocampal NMDAR-dependent information processing.

DISCUSSION

In this study, we identified AETA as a novel activity-dependent modulator of NMDARs that competes with the co-agonists glycine/D-serine. Our findings provide compelling evidence that AETA is capable of modifying the conformation of NMDARs and possesses a unique dual role as a molecular key. It reduces NMDAR ionotropic activity and associated calcium-dependent signaling, while concurrently promoting ion-flux-independent activity, thereby permitting LTD of synapse strength, and facilitates spine shrinkage. A diagram is shown in Figure S15, where we summarize this new AETA-dependent NMDAR activation mechanism. While numerous molecules have been identified as NMDAR modulators,[27,28] to the best of our knowledge, none exhibit the distinct dual property observed with AETA. In fact, until this discovery, no molecule with the property to activate the ion-flux-independent mode of NMDAR signaling had ever been identified. Through our knockout strategy utilizing the APPdelETA mouse model and subsequent rescue experiments via acute application or *in vivo* expression of AETA, we have demonstrated that AETA controls ionic NMDAR function and is both necessary and sufficient for maintaining adequate non-ionotropic NMDAR function that permits LTD at the CA3–CA1 synapse and adequate memory processing. Given that APP, the precursor of AETA, is among the most abundant proteins in synaptic boutons,[29] it occupies an ideal position as a reservoir for AETA, allowing for this activity-dependent neuromodulatory function.

AETA exerts a depressive effect on NMDAR current and calcium influx within spines. This ionotropic activity holds critical importance for synaptic integration and LTP, which in turn have far-reaching implications for dendritic computations,[30] sensory perception,[31] and adaptations to neuronal representations.[32] Consequently, the release of AETA as a neuromodulator may have broad impacts on neuronal function, influencing various aspects of behavior. Our findings demonstrate that AETA levels regulate the frequency of NMDAR-mediated sEPSCs without affecting their amplitude. Notably, the modulation of AETA levels does not alter AMPAR sEPSCs or the PPR. These observations suggest that AETA specifically modulates the activity of distinct NMDAR-only clusters (silent synapses), although the precise identity and position of these clusters remains unknown, representing an intriguing area for future investigation. Pharmacological analysis suggests that AETA preferably inhibits NMDARs containing the GluN2A subunit, but future work will be essential to identify its inhibitory activity on the multitude of heteromeric NMDARs.

The importance of the ion-flux-independent activity of NMDAR for LTD remains a subject of debate.[5,8,10,11,14] Our findings provide a potential explanation for these conflicting reports, as the observation of non-ionotropic signaling of NMDARs may be dependent on the degree of AETA release and its competitive interaction with glycine/D-serine, which might depend on the experimental preparations. Furthermore, data obtained from the APPdelETA mouse model suggest that the mechanisms underlying LTP and LTD can be further dissociated, with AETA being necessary for the induction of LTD but not essential for LTP induction or expression. However, it should be noted that we previously observed a partial inhibition of LTP upon the application of AETA to control slices.[15,16] In physiological conditions, it is plausible that an acute increase in AETA levels would result in a subset of NMDARs being driven into an LTD-prone state due to reduced co-agonist binding. As a consequence, these NMDARs become less available to contribute to LTP, thereby reducing the capacity of these synapses to express LTP. Our argument finds strong support in our data on spine shrinkage, where AETA transforms the expected spine growth into spine shrinkage. While we did not directly show that AETA-induced spine shrinkage is independent of ion flux via NMDARs, this AETA effect is identical to what has been observed in the presence of pharmacological antagonists of the glycine/D-serine binding site, 7CK and L698,560,[12,20] and there is strong evidence that this action is driven by ion-flux-independent NMDAR signaling and mediated by phosphorylation of p38, which is increased by AETA.

Our findings contribute to the growing body of evidence linking APP to NMDAR function, including NMDAR alterations observed during aging.[17,25,33,34] However, there is still limited information regarding the role of AETA in pathological mechanisms. Given the close association between APP processing and the etiology of Alzheimer's disease (AD),[35] there is emerging evidence suggesting that AETA might accumulate in patients with AD.[16,36] With the discovery of this newly identified AETA-driven mechanism, it becomes crucial to investigate whether it contributes to NMDAR-dependent synapse dysfunction and spine loss, both of which are considered early events in AD progression.[37–39] Moreover, beyond AD, the endogenous mechanism of action of AETA on NMDARs identified in our study could be disrupted in various other neurodegenerative, neurological, and psychiatric disorders involving this receptor. For instance, abnormal NMDAR function has been implicated in neurodegenerative diseases such as Parkinson's and Huntington's diseases,[40,41] traumatic brain injury,[42] stroke,[43] epilepsy,[44] autism spectrum disorder and intellectual disability,[45] anti-NMDA receptor encephalitis and anti-GluN2 antibodies associated with systemic lupus erythematosus,[46] schizophrenia, and depression.[47] Our discovery provides the impetus to explore the potential involvement of AETA-driven regulation of NMDARs in the pathophysiology of these disorders.

STAR★METHODS

Detailed methods are provided in the online version of this paper and include the following:

- KEY RESOURCES TABLE
- RESOURCE AVAILABILITY
  - ○ Lead contact
  - ○ Materials availability
  - ○ Data and code availability
- EXPERIMENTAL MODEL AND STUDY PARTICIPANT DETAILS
  - ○ Oocytes
  - ○ Mice and rats
  - ○ Primary neuronal cultures
- METHOD DETAILS
  - ○ Peptides
  - ○ Electrophysiology in *Xenopus* oocytes
  - ○ Electrophysiology and p38 activity in neuronal cultures
  - ○ Electrophysiology in hippocampal slices
  - ○ uEPSP and calcium transients in single spines
  - ○ FLIM-FRET of GluN1-GFP/GluN1-mCherry FRET pair
  - ○ Two-photon imaging of spine structural plasticity
  - ○ BACE1 inhibition *in vivo*
  - ○ *In vivo* neuronal activation or inhibition by DREADD
  - ○ Generation of APPdelETA mice
  - ○ Generation of AETA-m mouse line
  - ○ Immunoblotting
  - ○ Golgi-Cox staining for spine density analysis
  - ○ Contextual fear conditioning
  - ○ Statistical analysis

SUPPLEMENTAL INFORMATION

Supplemental information can be found online at https://doi.org/10.1016/j.neuron.2024.05.027.

ACKNOWLEDGMENTS

Complementary DNA (cDNA) for expression of recombinant rodent NMDARs in oocytes were generously provided by Dr. Paoletti (Institut de Biologie de l'Ecole Normale Supérieure [IBENS], France). cDNA for expression of recombinant AMPARs in oocytes were generously provided by Dr. Kristensen (University of Copenhagen, Denmark). We thank Franck Chatelain (IPMC, France) for technical help with *Xenopus* oocyte recordings. We thank Maxime Villet (IPMC, France) for technical help with pictures of virus spread. We thank Prof. Haass (German Center for Neurodegenerative Diseases Munich; Biomedical Center, Division of Metabolic Biochemistry, Faculty of Medicine, Ludwig-Maximilians-Universität München, Germany) for financial support and insightful discussions. This work was supported by the Centre National de la Recherche Scientifique (CNRS); the French Association France Alzheimer (AAP SM 2018 Dossier 1795) to H.M.; the French Fondation Alzheimer (AAP 2015 AETAPHYS) to H.M.; the Agence Nationale de la Recherche (ANR-21-CE16-0032 APPYSYNAPSE) to H.M. and L.G.; the Flag ERA JTC 2019 (MILEDI Project) to S.M. and H.M.; the Investments for the Future LABEX SIGNALIFE #ANR-11-LABX-0028-01 to M.M.; the Fondation pour la Recherche Médicale (FRM) to L.G.; the European Research Council Synergy grant (ENSEMBLE, #951294) to L.G.; the Institut Neuromod, Université Côte d'Azur, to H.M. and J.R.M.; the MRC (1514380) and EUFP17 Marie Curie Actions (PCIG10-GA-2011-303680) to M.C.A.; the Wellcome Trust (101029/Z/13/Z) to J.R.M.; the BBSRC (BB/R002177/1) to M. Amici; the NIH (R01 NS062736) to K.Z.; and the Deutsche Forschungsgemeinschaft Walter Benjamin project (468470832) to M. Anisimova. J. Dunot is the recipient of a PhD fellowship from the Ministère de la Recherche, de l'Enseignement Supérieur et de l'Innovation.

AUTHOR CONTRIBUTIONS

J. Dunot, S.M., P.A.P., M.M., and H.M. performed electrophysiological analysis by field and patch clamp in hippocampal slices. A.W., B.L., C. Gandin, and H.M. performed analysis on *Xenopus* oocytes. J. Dunot, I.B., and H.M. performed stereotaxic surgeries. M. Amici, M.C.A., and J.R.M. performed analysis of EPSP combined with calcium transients in hippocampal slices. J. Dupuis, M.U., and L.G. performed analysis of NMDAR conformation by FRET. M. Anisimova, S.J.P., and K.Z. performed analysis of spine structural plasticity. C. Giudici, M.W., H.H., J. Dunot, and H.M. performed all analysis by immunoblotting. C. Gandin performed spine density analysis. M.W., B.W., R.N., and W.W. created the APPdelETA and AETA-m mouse lines. J. Dunot performed behavioral analysis. H.M. supervised the full study and wrote the manuscript with help from other authors.

DECLARATION OF INTERESTS

The authors declare no competing interests.

DECLARATION OF GENERATIVE AI AND AI-ASSISTED TECHNOLOGIES IN THE WRITING PROCESS

During the preparation of this work, the senior author used ChatGPT in order to improve readability and language. After using this tool, the author reviewed and edited the content as needed and takes full responsibility for the content of the publication.

Received: July 26, 2023
Revised: April 9, 2024
Accepted: May 29, 2024
Published: June 14, 2024

REFERENCES

1. Dupuis, J.P., Nicole, O., and Groc, L. (2023). NMDA receptor functions in health and disease: Old actor, new dimensions. Neuron *111*, 2312–2328. https://doi.org/10.1016/j.neuron.2023.05.002.
2. Lüscher, C., and Malenka, R.C. (2012). NMDA receptor-dependent long-term potentiation and long-term depression (LTP/LTD). Cold Spring Harb. Perspect. Biol. *4*, a005710. https://doi.org/10.1101/cshperspect.a005710.
3. Paoletti, P., Bellone, C., and Zhou, Q. (2013). NMDA receptor subunit diversity: impact on receptor properties, synaptic plasticity and disease. Nat. Rev. Neurosci. *14*, 383–400. https://doi.org/10.1038/nrn3504.
4. Hansen, K.B., Yi, F., Perszyk, R.E., Furukawa, H., Wollmuth, L.P., Gibb, A.J., and Traynelis, S.F. (2018). Structure, function, and allosteric modulation of NMDA receptors. J. Gen. Physiol. *150*, 1081–1105. https://doi.org/10.1085/jgp.201812032.

5. Dore, K., Stein, I.S., Brock, J.A., Castillo, P.E., Zito, K., and Sjöström, P.J. (2017). Unconventional NMDA Receptor Signaling. J. Neurosci. *37*, 10800–10807. https://doi.org/10.1523/JNEUROSCI.1825-17.2017.
6. Dore, K., Aow, J., and Malinow, R. (2016). The Emergence of NMDA Receptor Metabotropic Function: Insights from Imaging. Front. Synaptic Neurosci. *8*, 20. https://doi.org/10.3389/fnsyn.2016.00020.
7. Dore, K., Aow, J., and Malinow, R. (2015). Agonist binding to the NMDA receptor drives movement of its cytoplasmic domain without ion flow. Proc. Natl. Acad. Sci. USA *112*, 14705–14710. https://doi.org/10.1073/pnas.1520023112.
8. Gray, J.A., Zito, K., and Hell, J.W. (2016). Non-ionotropic signaling by the NMDA receptor: controversy and opportunity. F1000Res. *5*, 1010. https://doi.org/10.12688/f1000research.8366.1.
9. Nabavi, S., Kessels, H.W., Alfonso, S., Aow, J., Fox, R., and Malinow, R. (2013). Metabotropic NMDA receptor function is required for NMDA receptor-dependent long-term depression. Proc. Natl. Acad. Sci. USA *110*, 4027–4032. https://doi.org/10.1073/pnas.1219454110.
10. Nabavi, S., Fox, R., Alfonso, S., Aow, J., and Malinow, R. (2014). GluA1 trafficking and metabotropic NMDA: addressing results from other laboratories inconsistent with ours. Philos. Trans. R. Soc. Lond. B Biol. Sci. *369*, 20130145. https://doi.org/10.1098/rstb.2013.0145.
11. Park, D.K., Stein, I.S., and Zito, K. (2022). Ion flux-independent NMDA receptor signaling. Neuropharmacology *210*, 109019. https://doi.org/10.1016/j.neuropharm.2022.109019.
12. Stein, I.S., Gray, J.A., and Zito, K. (2015). Non-Ionotropic NMDA Receptor Signaling Drives Activity-Induced Dendritic Spine Shrinkage. J. Neurosci. *35*, 12303–12308. https://doi.org/10.1523/JNEUROSCI.4289-14.2015.
13. Stein, I.S., Park, D.K., Claiborne, N., and Zito, K. (2021). Non-ionotropic NMDA receptor signaling gates bidirectional structural plasticity of dendritic spines. Cell Rep. *34*, 108664. https://doi.org/10.1016/j.celrep.2020.108664.
14. Babiec, W.E., Guglietta, R., Jami, S.A., Morishita, W., Malenka, R.C., and O'Dell, T.J. (2014). Ionotropic NMDA receptor signaling is required for the induction of long-term depression in the mouse hippocampal CA1 region. J. Neurosci. *34*, 5285–5290. https://doi.org/10.1523/JNEUROSCI.5419-13.2014.
15. Mensch, M., Dunot, J., Yishan, S.M., Harris, S.S., Blistein, A., Avdiu, A., Pousinha, P.A., Giudici, C., Busche, M.A., Jedlicka, P., et al. (2021). Aη-α and Aη-β peptides impair LTP ex vivo within the low nanomolar range and impact neuronal activity in vivo. Alzheimer's Res. Ther. *13*, 125. https://doi.org/10.1186/s13195-021-00860-1.
16. Willem, M., Tahirovic, S., Busche, M.A., Ovsepian, S.V., Chafai, M., Kootar, S., Hornburg, D., Evans, L.D.B., Moore, S., Daria, A., et al. (2015). η-Secretase processing of APP inhibits neuronal activity in the hippocampus. Nature *526*, 443–447. https://doi.org/10.1038/nature14864.
17. Pousinha, P.A., Mouska, X., Raymond, E.F., Gwizdek, C., Dhib, G., Poupon, G., Zaragosi, L.-E., Giudici, C., Bethus, I., Pacary, E., et al. (2017). Physiological and pathophysiological control of synaptic GluN2B-NMDA receptors by the C-terminal domain of amyloid precursor protein. eLife *6*, e25659. https://doi.org/10.7554/eLife.25659.
18. Papouin, T., Ladépêche, L., Ruel, J., Sacchi, S., Labasque, M., Hanini, M., Groc, L., Pollegioni, L., Mothet, J.-P., and Oliet, S.H.R. (2012). Synaptic and extrasynaptic NMDA receptors are gated by different endogenous coagonists. Cell *150*, 633–646. https://doi.org/10.1016/j.cell.2012.06.029.
19. Ferreira, J.S., Papouin, T., Ladépêche, L., Yao, A., Langlais, V.C., Bouchet, D., Dulong, J., Mothet, J.-P., Sacchi, S., Pollegioni, L., et al. (2017). Co-agonists differentially tune GluN2B-NMDA receptor trafficking at hippocampal synapses. eLife *6*, e25492. https://doi.org/10.7554/eLife.25492.
20. Stein, I.S., Park, D.K., Flores, J.C., Jahncke, J.N., and Zito, K. (2020). Molecular Mechanisms of Non-ionotropic NMDA Receptor Signaling in Dendritic Spine Shrinkage. J. Neurosci. *40*, 3741–3750. https://doi.org/10.1523/JNEUROSCI.0046-20.2020.
21. Aow, J., Dore, K., and Malinow, R. (2015). Conformational signaling required for synaptic plasticity by the NMDA receptor complex. Proc. Natl. Acad. Sci. USA *112*, 14711–14716. https://doi.org/10.1073/pnas.1520029112.
22. Oh, W.C., Hill, T.C., and Zito, K. (2013). Synapse-specific and size-dependent mechanisms of spine structural plasticity accompanying synaptic weakening. Proc. Natl. Acad. Sci. USA *110*, E305–E312. https://doi.org/10.1073/pnas.1214705110.
23. Zhou, Q., Homma, K.J., and Poo, M.-m. (2004). Shrinkage of dendritic spines associated with long-term depression of hippocampal synapses. Neuron *44*, 749–757. https://doi.org/10.1016/j.neuron.2004.11.011.
24. Park, D.K., Petshow, S., Anisimova, M., Barragan, E.V., Gray, J.A., Stein, I.S., and Zito, K. (2022). Reduced d-serine levels drive enhanced non-ionotropic NMDA receptor signaling and destabilization of dendritic spines in a mouse model for studying schizophrenia. Neurobiol. Dis. *170*, 105772. https://doi.org/10.1016/j.nbd.2022.105772.
25. Rajão-Saraiva, J., Dunot, J., Ribera, A., Temido-Ferreira, M., Coelho, J.E., König, S., Moreno, S., Enguita, F.J., Willem, M., Kins, S., et al. (2023). Age-dependent NMDA receptor function is regulated by the amyloid precursor protein. Aging Cell *22*, e13778. https://doi.org/10.1111/acel.13778.
26. Marie, H., Morishita, W., Yu, X., Calakos, N., and Malenka, R.C. (2005). Generation of silent synapses by acute in vivo expression of CaMKIV and CREB. Neuron *45*, 741–752.
27. Ahmed, H., Haider, A., and Ametamey, S.M. (2020). N-Methyl-D-Aspartate (NMDA) receptor modulators: a patent review (2015-present). Expert Opin. Ther. Pat. *30*, 743–767. https://doi.org/10.1080/13543776.2020.1811234.
28. Geoffroy, C., Paoletti, P., and Mony, L. (2022). Positive allosteric modulation of NMDA receptors: mechanisms, physiological impact and therapeutic potential. J. Physiol. *600*, 233–259. https://doi.org/10.1113/JP280875.
29. Wilhelm, B.G., Mandad, S., Truckenbrodt, S., Kröhnert, K., Schäfer, C., Rammner, B., Koo, S.J., Claßen, G.A., Krauss, M., Haucke, V., et al. (2014). Composition of isolated synaptic boutons reveals the amounts of vesicle trafficking proteins. Science *344*, 1023–1028. https://doi.org/10.1126/science.1252884.
30. Richards, B.A., Lillicrap, T.P., Beaudoin, P., Bengio, Y., Bogacz, R., Christensen, A., Clopath, C., Costa, R.P., de Berker, A., Ganguli, S., et al. (2019). A deep learning framework for neuroscience. Nat. Neurosci. *22*, 1761–1770. https://doi.org/10.1038/s41593-019-0520-2.
31. Takahashi, N., Oertner, T.G., Hegemann, P., and Larkum, M.E. (2016). Active cortical dendrites modulate perception. Science *354*, 1587–1590. https://doi.org/10.1126/science.aah6066.
32. Bittner, K.C., Milstein, A.D., Grienberger, C., Romani, S., and Magee, J.C. (2017). Behavioral time scale synaptic plasticity underlies CA1 place fields. Science *357*, 1033–1036. https://doi.org/10.1126/science.aan3846.
33. Cousins, S.L., Hoey, S.E.A., Anne Stephenson, F., and Perkinton, M.S. (2009). Amyloid precursor protein 695 associates with assembled NR2A- and NR2B-containing NMDA receptors to result in the enhancement of their cell surface delivery. J. Neurochem. *111*, 1501–1513. https://doi.org/10.1111/j.1471-4159.2009.06424.x.
34. Hoe, H.-S., Fu, Z., Makarova, A., Lee, J.-Y., Lu, C., Feng, L., Pajoohesh-Ganji, A., Matsuoka, Y., Hyman, B.T., Ehlers, M.D., et al. (2009). The effects of amyloid precursor protein on postsynaptic composition and activity. J. Biol. Chem. *284*, 8495–8506. https://doi.org/10.1074/jbc.M900141200.
35. Haass, C., Kaether, C., Thinakaran, G., and Sisodia, S. (2012). Trafficking and proteolytic processing of APP. Cold Spring Harb. Perspect. Med. *2*, a006270. https://doi.org/10.1101/cshperspect.a006270.
36. García-Ayllón, M.S., Lopez-Font, I., Boix, C.P., Fortea, J., Sánchez-Valle, R., Lleó, A., Molinuevo, J.-L., Zetterberg, H., Blennow, K., and Sáez-Valero, J. (2017). C-terminal fragments of the amyloid precursor protein in cerebrospinal fluid as potential biomarkers for Alzheimer disease. Sci. Rep. *7*, 2477. https://doi.org/10.1038/s41598-017-02841-7.

37. Knobloch, M., and Mansuy, I.M. (2008). Dendritic spine loss and synaptic alterations in Alzheimer's disease. Mol. Neurobiol. *37*, 73–82. https://doi.org/10.1007/s12035-008-8018-z.

38. Malinow, R. (2012). New developments on the role of NMDA receptors in Alzheimer's disease. Curr. Opin. Neurobiol. *22*, 559–563. https://doi.org/10.1016/j.conb.2011.09.001.

39. Selkoe, D.J. (2002). Alzheimer's disease is a synaptic failure. Science *298*, 789–791.

40. Parsons, M.P., and Raymond, L.A. (2014). Extrasynaptic NMDA Receptor Involvement in Central Nervous System Disorders. Neuron *82*, 279–293. https://doi.org/10.1016/j.neuron.2014.03.030.

41. Wang, J., Wang, F., Mai, D., and Qu, S. (2020). Molecular Mechanisms of Glutamate Toxicity in Parkinson's Disease. Front. Neurosci. *14*, 585584. https://doi.org/10.3389/fnins.2020.585584.

42. Khormali, M., Heidari, S., Ahmadi, S., Arab Bafrani, M., Baigi, V., and Sharif-Alhoseini, M. (2022). N-methyl-D-aspartate receptor antagonists in improving cognitive deficits following traumatic brain injury: a systematic review. Brain Inj. *36*, 1071–1088. https://doi.org/10.1080/02699052.2022.2109749.

43. Wu, Q.J., and Tymianski, M. (2018). Targeting NMDA receptors in stroke: new hope in neuroprotection. Mol. Brain *11*, 15. https://doi.org/10.1186/s13041-018-0357-8.

44. Hanada, T. (2020). Ionotropic Glutamate Receptors in Epilepsy: A Review Focusing on AMPA and NMDA Receptors. Biomolecules *10*, 464. https://doi.org/10.3390/biom10030464.

45. Vieira, M.M., Jeong, J., and Roche, K.W. (2021). The role of NMDA receptor and neuroligin rare variants in synaptic dysfunction underlying neurodevelopmental disorders. Curr. Opin. Neurobiol. *69*, 93–104. https://doi.org/10.1016/j.conb.2021.03.001.

46. Wollmuth, L.P., Chan, K., and Groc, L. (2021). The diverse and complex modes of action of anti-NMDA receptor autoantibodies. Neuropharmacology *194*, 108624. https://doi.org/10.1016/j.neuropharm.2021.108624.

47. Adell, A. (2020). Brain NMDA Receptors in Schizophrenia and Depression. Biomolecules *10*, 947. https://doi.org/10.3390/biom10060947.

48. Platzer, K., Yuan, H., Schütz, H., Winschel, A., Chen, W., Hu, C., Kusumoto, H., Heyne, H.O., Helbig, K.L., Tang, S., et al. (2017). GRIN2B encephalopathy: novel findings on phenotype, variant clustering, functional consequences and treatment aspects. J. Med. Genet. *54*, 460–470. https://doi.org/10.1136/jmedgenet-2016-104509.

49. Mony, L., Zhu, S., Carvalho, S., and Paoletti, P. (2011). Molecular basis of positive allosteric modulation of GluN2B NMDA receptors by polyamines. EMBO J. *30*, 3134–3146. https://doi.org/10.1038/emboj.2011.203.

50. Stenum-Berg, C., Musgaard, M., Chavez-Abiega, S., Thisted, C.L., Barrella, L., Biggin, P.C., and Kristensen, A.S. (2019). Mutational Analysis and Modeling of Negative Allosteric Modulator Binding Sites in AMPA Receptors. Mol. Pharmacol. *96*, 835–850. https://doi.org/10.1124/mol.119.116871.

51. Doré, K., Labrecque, S., Tardif, C., and De Koninck, P. (2014). FRET-FLIM investigation of PSD95-NMDA receptor interaction in dendritic spines; control by calpain, CaMKII and Src family kinase. PLoS One *9*, e112170. https://doi.org/10.1371/journal.pone.0112170.

52. Chatelain, F.C., Bichet, D., Douguet, D., Feliciangeli, S., Bendahhou, S., Reichold, M., Warth, R., Barhanin, J., and Lesage, F. (2012). TWIK1, a unique background channel with variable ion selectivity. Proc. Natl. Acad. Sci. USA *109*, 5499–5504. https://doi.org/10.1073/pnas.1201132109.

53. Laube, B., Hirai, H., Sturgess, M., Betz, H., and Kuhse, J. (1997). Molecular determinants of agonist discrimination by NMDA receptor subunits: analysis of the glutamate binding site on the NR2B subunit. Neuron *18*, 493–503. https://doi.org/10.1016/s0896-6273(00)81249-0.

54. Liao, D., Hessler, N.A., and Malinow, R. (1995). Activation of postsynaptically silent synapses during pairing-induced LTP in CA1 region of hippocampal slice. Nature *375*, 400–404. https://doi.org/10.1038/375400a0.

55. Wong, J.M., and Gray, J.A. (2018). Long-Term Depression Is Independent of GluN2 Subunit Composition. J. Neurosci. *38*, 4462–4470. https://doi.org/10.1523/JNEUROSCI.0394-18.2018.

56. Ashby, M.C., and Isaac, J.T.R. (2011). Maturation of a recurrent excitatory neocortical circuit by experience-dependent unsilencing of newly formed dendritic spines. Neuron *70*, 510–521. https://doi.org/10.1016/j.neuron.2011.02.057.

57. Bard, L., Sainlos, M., Bouchet, D., Cousins, S., Mikasova, L., Breillat, C., Stephenson, F.A., Imperiali, B., Choquet, D., and Groc, L. (2010). Dynamic and specific interaction between synaptic NR2-NMDA receptor and PDZ proteins. Proc. Natl. Acad. Sci. USA *107*, 19561–19566. https://doi.org/10.1073/pnas.1002690107.

58. Kellermayer, B., Ferreira, J.S., Dupuis, J., Levet, F., Grillo-Bosch, D., Bard, L., Linarès-Loyez, J., Bouchet, D., Choquet, D., Rusakov, D.A., et al. (2018). Differential Nanoscale Topography and Functional Role of GluN2-NMDA Receptor Subtypes at Glutamatergic Synapses. Neuron *100*, 106–119.e7. https://doi.org/10.1016/j.neuron.2018.09.012.

59. Feng, G., Mellor, R.H., Bernstein, M., Keller-Peck, C., Nguyen, Q.T., Wallace, M., Nerbonne, J.M., Lichtman, J.W., and Sanes, J.R. (2000). Imaging neuronal subsets in transgenic mice expressing multiple spectral variants of GFP. Neuron *28*, 41–51. https://doi.org/10.1016/s0896-6273(00)00084-2.

60. Woods, G.F., Oh, W.C., Boudewyn, L.C., Mikula, S.K., and Zito, K. (2011). Loss of PSD-95 enrichment is not a prerequisite for spine retraction. J. Neurosci. *31*, 12129–12138. https://doi.org/10.1523/JNEUROSCI.6662-10.2011.

61. Fernandez, S.P., Broussot, L., Marti, F., Contesse, T., Mouska, X., Soiza-Reilly, M., Marie, H., Faure, P., and Barik, J. (2018). Mesopontine cholinergic inputs to midbrain dopamine neurons drive stress-induced depressive-like behaviors. Nat. Commun. *9*, 4449. https://doi.org/10.1038/s41467-018-06809-7.

62. Wefers, B., Bashir, S., Rossius, J., Wurst, W., and Kühn, R. (2017). Gene editing in mouse zygotes using the CRISPR/Cas9 system. Methods *121–122*, 55–67. https://doi.org/10.1016/j.ymeth.2017.02.008.

63. Haeussler, M., Schönig, K., Eckert, H., Eschstruth, A., Mianné, J., Renaud, J.-B., Schneider-Maunoury, S., Shkumatava, A., Teboul, L., Kent, J., et al. (2016). Evaluation of off-target and on-target scoring algorithms and integration into the guide RNA selection tool CRISPOR. Genome Biol. *17*, 148. https://doi.org/10.1186/s13059-016-1012-2.

Please cite this article in press as: Dunot et al., APP fragment controls both ionotropic and non-ionotropic signaling of NMDA receptors, Neuron (2024), https://doi.org/10.1016/j.neuron.2024.05.027

STAR★METHODS

KEY RESOURCES TABLE

REAGENT or RESOURCE	SOURCE	IDENTIFIER
Antibodies		
Anti-rabbit-IgG-HRP conjugated secondary antibody	Jackson ImmunoResearch	Cat#111-036-045; RRID: AB_2337943
Anti-rat-IgG-HRP conjugated secondary antibody	Jackson ImmunoResearch	Cat#111-036-062; RRID: AB_2338142
Anti-mouse-IgG-HRP conjugated secondary antibody	Jackson ImmunoResearch	Cat#111-036-146; RRID: AB_2307347
M3.2	Biolegend	Cat#805701; RRID: AB_2564981
2D8	Sigma-Aldrich	Cat#MABN2273
2E9	Sigma-Aldrich	Cat#MABN2295
22C11	Merck Milipore	Cat#MAB348
Y188	Abcam	Cat#ab32136; RRID: AB_2289606
mCherry	Takara	Cat#632496; RRID: AB_10013483
Synaptophysin	Sigma-Aldrich	Cat#S5786
Synaptobrevin-2	SYSY	Cat#104211
p-38	Cell Signaling	Cat#8690; RRID: AB_10999090
p-p38	Cell Signaling	Cat#9216; RRID: AB_331296
Beta-actin	Sigma-Aldrich	Cat#AC-74
Bacterial and virus strains		
AAV8-hSyn-hM3Dq-mCherry	Addgene	Cat#50474
AAV8-hSyn-hM4Di-mCherry	Addgene	Cat#50475
Chemicals, peptides, and recombinant proteins		
Glycine	Euromedex	Cat#26128 6405
L-Glutamate	Sigma-Aldrich	Cat#1446600 USP
Cyclothiazide	Biothechne	Cat#07130-50
Poly-L-Lysine	Sigma Aldrich	Cat#P2636
Neurobasal medium (Gibco)	Thermo Fisher Scientific	Cat#21103049
B27	Thermo Fisher Scientific	Cat#17504044
GlutaMAX	Thermo Fisher Scientific	Cat#35050061
Penicillin/streptomycin	Thermo Fisher Scientific	Cat#15140122
NaCl	Sigma Aldrich	Cat#560 14
KCl	Sigma Aldrich	Cat#P3911
CaCl2	Sigma Aldrich	Cat#C8106
HEPES	Sigma Aldrich	Cat#H3375
Glucose	VWR	Cat#24379294
Tetrodotoxin	Alomone Labs	Cat#T-550
Cs-gluconate (Cesium Hydroxide)	Sigma Aldrich	Cat#232041
CsCl	Sigma Aldrich	Cat#289329
TEACl	Sigma Aldrich	Cat#86614
EGTA	Sigma Aldrich	Cat#E3889
MgATP	Sigma Aldrich	Cat#A9187
NaGTP	Sigma Aldrich	Cat#G8877
NMDA	Tocris	Cat#0114
Sucrose	Sigma Aldrich	Cat#S0389

(*Continued on next page*)

Please cite this article in press as: Dunot et al., APP fragment controls both ionotropic and non-ionotropic signaling of NMDA receptors, Neuron (2024), https://doi.org/10.1016/j.neuron.2024.05.027

Continued

REAGENT or RESOURCE	SOURCE	IDENTIFIER
NaH2PO4	Sigma Aldrich	Cat#S9638
$MgSO_4$	Sigma Aldrich	Cat#230391
$NaHCO_3$	Sigma Aldrich	Cat#S6014
Gluconic acid (potassium salt: K-gluconate)	Sigma Aldrich	Cat#G1951
$MgCl_2$	Sigma Aldrich	Cat#M2670
Picrotoxin	Sigma Aldrich	Cat#P1675
DNQX	Tocris	Cat#2312
D-APV	Tocris	Cat#0106
NBQX	Tocris	Cat#0373
Cesium-methanesulfonate (Methanesulfonate)	Sigma Aldrich	Cat#64285
Na_2ATP	Sigma Aldrich	Cat#A26209
cAMP	Sigma Aldrich	Cat#A9501
MK801	Sigma Aldrich	Cat#M107
L689,560	Tocris	Cat#0742
Alexa Fluor 594 hydrazide	Invitrogen	Cat#A10438
Fluo-4 pentapotassium salt	Invitrogen	Cat#F14200
Fluo-5F pentapotassium salt	Invitrogen	Cat#F14221
MNI-caged-L-glutamate	Tocris	Cat#1490
Trolox	Sigma	Cat#238813
BrainPhys medium	STEMCELL Technologies	Cat#O5790
Ketamine	Virbac	Ketamine 1000
Xylazine	Virbac	Paxman
LY2811376	Clinisciences	Cat#HY-10472
40% PEG300	Fluka	Cat#81160
5% Tween-80	Sigma-Aldrich	Cat#P1754
CNO	Enzo	Cat#BML-NS105-0025
Acepromazine	N/A	Calmivet
Hyaluronidase	Sigma-Aldrich	Cat#H4272
Diethylamine	Sigma-Aldrich	Cat#471216-5mL
Tris-HCl	VWR	Cat#0234-500G
Na_2EDTA	Sigma-Aldrich	Cat#E6758-100g
NP-40 nonidet	Roche	Cat#1175459900
Sodium deoxycholate	Sigma-Aldrich	Cat#D5670-25g
Triton X-100	Sigma-Aldrich	Cat#X100
Protease inhibitors	Sigma-Aldrich	Cat#P8340
Bradford	Biorad	Cat#5000205
Tris-Tricine gels	Invitrogen	Cat#EC66252BOX
I-Block	Thermo Fisher Scientific	Cat#T2015
Tween 20 merck	Sigma-Aldrich	Cat#102423676
Ponceau	Sigma-Aldrich	Cat#P71-70
Chemiluminescence detection reagent ECL	Perkin Elmer	Cat#NEL112001EA
TCN201	Tocris	Cat#4154
DMSO	Sigma-Aldrich	Cat#D8418
Ifenprodil	Sigma Aldrich	Cat#I2892
D-Serine	Sigma Aldrich	Cat#S4250
Critical commercial assays		
Human/Rat (Mouse) β-Amyloid (40) ELISA Kit	Wako	Cat#294-62501

(*Continued on next page*)

Please cite this article in press as: Dunot et al., APP fragment controls both ionotropic and non-ionotropic signaling of NMDA receptors, Neuron (2024), https://doi.org/10.1016/j.neuron.2024.05.027

Continued

REAGENT or RESOURCE	SOURCE	IDENTIFIER
Golgi-Cox FD rapid GolgiStain kit, FD Neurotechnologies, USA	FD Neurotechnologies	Golgi stain
Experimental models: Organisms/strains		
APPdelETA mice	DZNE Munich -B6J-App<em1Bwef> (+em3)	private MGI: 7281307 (under registration at Jackson Laboratories)
AETA-m mice	LMU Munich -Tg(Thy1-APP)A2haa	private MGI: 7281720 (under registration at Jackson Laboratories)
C57BL/6	Charles River	RRID: IMSR_JAX:000664
Oligonucleotides		
APPintron11-12for	Eurogentec	AAGCTCTGACTTTCCTTAAGGTGC
APPintron12-13rev	Eurogentec	TAGGAGTGGTATCCCTGCGGGT
AETA	Peptide Specialty Laboratories (PSL GmbH), Munich, Germany	MISEPRISYGNDALMPSLTETKTTVELLPVNGEFSLDDLQPWHSFGADSVPANTENEVEPVDARPAADRGLTTRPGSGLTNIKTEEISEVKMDAEFRHDSGYEVHHQK
CtrlP	Peptide Specialty Laboratories (PSL GmbH), Munich, Germany	KQHHVEYGSDHRFEADMKVESIEETKINTLGSGPRTTLGRDAAPRADVPEVENETNAPVSDAGFSHWPQLDDLSFEGNVPLLEVTTKTETLSPMLADNGYSIRPESIM
crRNA APP-Ex12dn	IDT	CGCTCTCATGCCTTCGCTGA
crRNA APP-Ex12up	IDT	AACTACTCCGACGATGTCT
Recombinant DNA		
Human GluN1-1a	Dr Laube, TU Darmstadt, Germany	Platzer et al.[48]
Human GluN2A	Dr Laube, TU Darmstadt, Germany	Platzer et al.[48]
Human GluN2B	Dr Laube, TU Darmstadt, Germany	Platzer et al.[48]
Rat GluN1-1a	Dr Paoletti, IBENS, France	Mony et al.[49]
Rat GluN2A	Dr Paoletti, IBENS, France	Mony et al.[49]
Rat GluN2B	Dr Paoletti, IBENS, France	Mony et al.[49]
Rat GluA1	Dr Kristensen, University of Copenhagen, Denmark	Stenum-Berg et al.[50]
Rat GluA2$_R$	Dr Kristensen, University of Copenhagen, Denmark	Stenum-Berg et al.[50]
Rat GluA3	Dr Kristensen, University of Copenhagen, Denmark	Stenum-Berg et al.[50]
GluN1-GFP	Dr De Koninck, CERVO Brain Research Center, Canada	Doré et al.[51]
GluN1-mCherry	Dr De Koninck, CERVO Brain Research Center, Canada	Doré et al.[51]
Flag-GluN2B	Dr Groc, IINS, France	Ferreira et al.[19]
Software and algorithms		
GraphPad Prism 9	Dotmatics	Academic module
Packwin; freezing module	Panlab	N/A
Clampfit 10.6	Axon Instruments	N/A
Clampex	Molecular Devices	N/A
Multiclamp	Molecular Devices	N/A

RESOURCE AVAILABILITY

Lead contact

Further information and requests for resources and reagents should be directed to and will be fulfilled by the lead contact, Hélène Marie (marie@ipmc.cnrs.fr).

Please cite this article in press as: Dunot et al., APP fragment controls both ionotropic and non-ionotropic signaling of NMDA receptors, Neuron (2024), https://doi.org/10.1016/j.neuron.2024.05.027

Materials availability

The new APPdelETA and AETA-m mouse lines have been preregistered to Jackson Laboratories for unrestricted availability upon publication.

Data and code availability

- All data reported in this paper will be shared by the lead contact upon request.
- This paper does not report original code.
- Any additional information required to reanalyze the data reported in this paper is available from the lead contact upon request.

EXPERIMENTAL MODEL AND STUDY PARTICIPANT DETAILS

Oocytes

Oocyte harvest was performed in accordance with the European directives 2010/63/EU on the Protection of Animals used for Scientific Purposes in the framework of project authorization APAFIS#14012–2018030214144339 as delivered by the competent French authorities and by the German local animal care and use committee (II25.3–19c20/15, RP Darmstadt, Germany).

Mice and rats

All experiments and protocols on mice and rats were performed in accordance with the European Communities' Council Directive 2010/63/EU. Protocols used in this study were approved by the committee for the Care and Use of Laboratory Animals and governments of the relevant countries as detailed in the relevant sections in the methods details below. The different mouse and rat species used are reported in the methods details where relevant. In all animal houses the rodents had *ad libitum* access to water (tap water) and standard chow and were maintained under constant environmental conditions (12:12 h light/dark cycle, 23 ± 2C and humidity of 55%). They were housed in groups of 5–6 animals by sex in standard cages (mouse: 542 cm^2; rat: 2065 cm^2) in animal houses under specific pathogen free (SPF) status. For *ex vivo* experiments, sex used is reported in each section whenever relevant. None of the mice used in the reported experiments were used in other previous non-reported *in vivo* procedures. For the behavioral experiment (Figures 4I–4K), only adult males (2–3 months old) were considered and the result cannot be generalized to both sexes for this experiment. AETA-m mice were backcrossed regularly (at least 8 times prior to experiments presented in this study) on C57BL6J background (Charles River) to obtain WT and transgenic mutants. APPdelETA homozygous and WT littermates were generated by crossing heterozygous male and female mice from different litters with intermittent backcrossing on C57BL6J background (Charles River) to obtain new heterozygous mice for the crossings. Littermates of the same sex were randomly assigned to experimental groups. Generation of double mutants (APPdelETA/AETA-m mice) was obtained in two steps. We first crossed homozygous male homozygous APPdelETA with female transgenic AETA-m mice. Upon obtaining heterozygous/transgenic females from this crossing, these females were bred with heterozygous APPdelETA males to obtain WT, homozygous and homozygous/transgenic genotypes from same litters for the behavioral experiment.

Primary neuronal cultures

E15 RjOrl:Swiss and E18 Sprague-Dawley rat embryos were used for neuronal cultures. Sex of embryos was not considered and both male and females embryos were used. Details of culture conditions are provided in relevant sections below.

METHOD DETAILS

Peptides

Synthetic AETA and control peptide (CtrlP, representing the reverse sequence of AETA) were obtained from Peptide Specialty Laboratories (PSL GmbH; Heidelberg, Germany) and consisted of the following sequences:

AETA sequence (108 amino acids):

MISEPRISYGNDALMPSLTETKTTVELLPVNGEFSLDDLQPWHSFGADSVPANTENEVEPVDARPAADRGLTTRPGSGLTNIKTEEISEVKMDAEFRHDSGYEVHHQK

CtrlP sequence (108 amino acids):

KQHHVEYGSDHRFEADMKVESIEETKINTLGSGPRTTLGRDAAPRADVPEVENETNAPVSDAGFSHWPQLDDLSFEGNVPLLEVTTKTETLSPMLADNGYSIRPESIM

The peptides were dissolved in dimethyl sulfoxide (DMSO) at 100 μM and placed at −80°C for long term storage. For recordings in *Xenopus* oocytes, these aliquots were further dissolved to 100 nM in oocyte recording solution on day of experiment. For all other experiments, the peptides were further diluted to 10 μM in artificial cerebrospinal fluid (aCSF) and placed at −80°C for long term storage. On day of experiment, aliquots were diluted to 10 nM in aCSF.

Electrophysiology in *Xenopus* oocytes

Human GluN1-1a (named GluN1 herein), GluN2A and GluN2B subunits of NMDAR (Laube lab)[48] or pcDNA3-based plasmids for rodent GluN1-1a, GluN2A and GluN2B subunits of NMDAR (Marie lab)[49] or pXOOF-based plasmids for rat GluA1, $GluA2_R$ and GluA3[50] were used for expression in *Xenopus* oocytes. All constructs were linearized with appropriate enzyme and transcribed into cRNA (mCAP mRNA Capping Kit, Ambion, or AmpliCap-Max T7 High Yield Message Maker KitA, TEBU). Oocytes from female *Xenopus laevis* were prepared as described previously.[52,53] *Xenopus laevis* oocytes were injected with 30 ng cRNAs in a volume of 50 nL of a 1:1 ratio of GluN1 per GluN2A or GluN2B, or 30 ng a 2:1 ratio of GluA2R per GluA1 or GluA3. 1–2 days after injection, two-electrode voltage clamp (TEVC) recording was performed at a holding potential of −60 mV or −70 mV at room temperature. The two microelectrodes were filled with 3M KCl and had a resistance of 0.5–1 MOhm. Currents were acquired at 200 Hz with a Geneclamp 500B amplifier, a Digidata 1322A digitizer and Clampex 9.2 software (Molecular Devices, USA). Recombinant NMDAR-mediated currents were induced in Mg^{2+}-free frog Ringer solution by co-application of L-glutamate (100 μM) and glycine (1 μM), unless otherwise indicated in figure caption. Recombinant AMPAR-mediated currents were induced by application of L-glutamate (300 μM) and cyclothiazide (CTZ, 100 μM). For determining dose-response relations, superfusion was switched to desired concentrations of peptides/drugs in Ringer solution. Glutamate/glycine, dissolved in bath solution, was applied either alone for 10 s (Laube lab) or 30 s (Marie lab) or after 15 s (Laube lab) or 1 min (Marie lab) pre-application of the appropriate peptide also dissolved in bath solution. Currents were measured with Clampfit 9.2 software (Molecular Devices, USA) and results were analyzed using GraphPad Prism version 9 (GraphPad, USA). 100% current value represented current obtained upon glutamate application prior to peptide application. Current value obtained after peptide application was normalized to this control current value for each oocyte recording. The dose-response curves of glutamate-induced peak currents were normalized to the maximal current value (Imax) obtained without AETA (Figure S1A) or with 100 μM glycine (Figure 1I). IC50 (half-maximal inhibitory concentration) and EC50 (half-maximal effective concentration) were calculated from fitting dose-response curves to a sigmoidal dose-response curve using the Hill equation. All experiments were from at least three batches of oocytes.

Electrophysiology and p38 activity in neuronal cultures

Primary hippocampal neurons were isolated from 15-day-old mouse embryo brain (E15) from RjOrl:Swiss pregnant female. Cells were mechanically dissociated and plated on 12-mm glass coverslips pre-treated with poly-L-Lysine (0.1 mg mL^{-1}; Sigma) and maintained at 37°C, 5% CO2 in Neurobasal medium (Gibco) supplemented with 2% B27 (Gibco), 2 mM GlutaMAX (Gibco) and 1% penicillin/streptomycin (10 000UI, 10 000 μg/mL; Gibco) for 10–14 days prior to use.

To test p38 activity, we incubated neurons (200,000 cells/sample) with AETA (10 nM) for 20 min. We collected control neurons and AETA-exposed neurons, lysed them in RIPA (see below) and processed the lysate for immunoblotting (see below).

Neurons were recorded in whole-cell patch-clamp configuration at −65 mV at room temperature (RT) in extracellular solution containing in mM: NaCl 150, KCl 2.5, $CaCl_2$ 2.0, HEPES 10, glucose 10 and glycine 0.01, pH 7,4 supplemented with Tetrodotoxin (100 nM) and NBQX (1μM). Recording pipettes (5–6 MΩ) were filled with Cs-gluconate solution (in mM): 117.5 Cs-gluconate, 15.5 CsCl, 10 TEACl, 8 NaCl, 10 HEPES, 0.25 EGTA, 4 MgATP and 0.3 NaGTP (pH 7.3; osmolarity 290–300 mOsm).

NMDA currents were evoked 5 times by 10 s application of 30 μM NMDA separated by 40 s washout (extracellular solution). After 10 min of peptide incubation (10 nM CtrlP or AETA in bath solution), neurons were stimulated again with another 5 pulses of NMDA application. Local application of NMDA was delivered by an automated perfusion system (ValveLink 8.2, Science Products) with a 350 μm tip that was set close to the cell of interest. For analysis, mean peak amplitude measured for the 5 stimulations before incubation was set as 100% current and a ratio amplitude was established on this mean for each evoked current. Two factor analysis of variance (two-way ANOVA) followed by Sidak's post-hoc was performed to analyze significance among the conditions.

Electrophysiology in hippocampal slices

For *ex vivo* electrophysiology recordings, 3–6 weeks old male RjOrl:SWISS mice (Janvier, France), 2–3 months male APPdelETA and WT littermates, or 3–4 weeks old male Sprague-Dawley rats (Janvier, France) were used. Mice were culled by cervical dislocation and hippocampi were dissected and incubated for 5 min in ice-cold oxygenated (95% O2/5% CO2) cutting solution (in mM): 234 sucrose, 2.5 KCl, 1.25 NaH_2PO_4, 10 $MgSO_4$, 0.5 $CaCl_2$, 26 $NaHCO_3$, 11 glucose (pH 7.4). Hippocampal slices (250 μm for patch-clamp recordings, 350 μm for field recordings) were cut on a vibratome (Microm HM600V, Thermo Scientific, France). For recovery, slices were then incubated in standard aCSF (in mM): 119 NaCl, 2.5 KCl, 1.25 NaH_2PO_4, 26 $NaHCO_3$, 1.3 $MgSO_4$, 2.5 $CaCl_2$ and 11 D-glucose, oxygenated with 95% O_2 and 5% CO_2, pH 7.4 for 1 h at 37 ± 1°C and then stored at RT until used for recordings. Recordings were done in this standard aCSF (unless otherwise stated) in a recording chamber on an upright microscope with IR-DIC illumination (SliceScope, Scientifica Ltd, UK) using a Multiclamp 700B amplifier (Molecular Devices, San Jose, CA, USA), under the control of pClamp10 software (Molecular Devices, San Jose, CA, USA). Data analysis was executed using Clampfit 10 software (Molecular Devices, San Jose, CA, USA). The Schaffer collateral pathway was stimulated at 0.1 Hz for patch clamp experiments and 0.25 Hz for field experiments (unless otherwise stated) using electrodes (glass pipettes filled with aCSF) placed in the stratum radiatum.

Patch-clamp experiments were performed at 31 ± 1°C. For whole-cell voltage-clamp, recording pipettes (5–6 MΩ) were filled with a solution containing the following: 117.5 mM Cs-gluconate, 15.5 mM CsCl, 10 mM TEACl, 8 mM NaCl, 10 HEPES, 0.25 mM EGTA, 4 mM MgATP and 0.3 NaGTP (pH 7.3; osmolarity 290–300 mOsm). For whole cell current-clamp, the recording pipette solution contained (in mM): 135 gluconic acid (potassium salt: K-gluconate), 5 NaCl, 2 $MgCl_2$, 10 HEPES, 0.5 EGTA, 2 MgATP and 0.4 NaGTP (pH 7.25; osmolarity 280–290 mOsm). After a tight seal (>1GΩ) on the cell body of the selected neuron was obtained, whole-cell patch clamp configuration was established, and cells were left to stabilize for 2–3 min before recordings began. Holding current and series

Please cite this article in press as: Dunot et al., APP fragment controls both ionotropic and non-ionotropic signaling of NMDA receptors, Neuron (2024), https://doi.org/10.1016/j.neuron.2024.05.027

CellPress
OPEN ACCESS

resistance were continuously monitored throughout the experiment, and if either of these two parameters varied by more than 20%, the cell was discarded.

NMDAR EPSCs were pharmacologically isolated by adding 50 μM picrotoxin (Sigma-Aldrich, dissolved in DMSO) to block GABAergic transmission and DNQX (10 μM; Sigma-Aldrich, dissolved in DMSO) to block AMPA receptors and recorded at +40mV. The time courses were obtained by normalizing each recording to the average value of all points constituting the first 10 min stable baseline. Graphs of current alteration was measured during the last 10 min of recording and calculated as % change from baseline average (first 10 min).

Spontaneous EPSCs were recorded at −65 mV in presence of picrotoxin (50 μM; Sigma-Aldrich), D-APV (50 μM; Tocris) for AMPAR EPSCs or NBQX (10 μM, Tocris) and Mg^{2+}-free aCSF for NMDA EPSCs using the following internal solution (mM): Cesium-methanesulfonate (143), NaCl (5), $MgCl_2$ (1), EGTA (1), $CaCl_2$ (0.3), HEPES (10), Na_2ATP (2), NaGTP (0.3) and cAMP (0.2) (pH 7.3 and 290–295 mOsm). To test effect of AETA or CtrlP (10 nM), sEPSC were first recorded in gap-free mode for 5 min (baseline condition), then the peptide was applied for 10 min, and sEPSC were then recorded for another 5 min (peptide condition). For recordings in WT and APPdelETA mice, 5 min were recorded for individual neurons of each genotype. In APPdelETA neurons, after these 5 min of recordings, AETA (10 nM) was bath applied for 10 min, after which another 5 min were recorded. Analysis of sEPSCs was performed on the first and last 5 min to compare frequencies and amplitudes use Clampfit 10. sEPSCs were detected manually by following criteria of peaks with a threshold 2xSD of baseline noise level and a faster rise time than decay time. Analysis was performed blind to experimental condition.

Minimal stimulation experiments were performed as described previously.[26] Briefly, EPSCs were recorded in CA1 neurons while stimulating the CA3 Schaffer collaterals in presence of picrotoxin (50 μM). After evoking a small (20–40 pA) EPSC at −65 mV at 0.1 Hz stimulation frequency, stimulation strength was reduced in small increments to the point that failures versus responses could be clearly distinguished visually. Stimulation intensity was then kept constant throughout experiment. 50 sweeps were recorded at −65 mV and 50 sweeps were recorded at +40 mV. Failures and success rates were estimated visually for each voltage by experimenter blind to genotype. Percent silent synapses were calculated as follows: $1 - \ln(F_{-65mV})/\ln(F_{+40mV})$ where F represents failure rate calculated for each voltage.[54]

Field excitatory postsynaptic potentials (fEPSPs) were recorded in the stratum radiatum of the CA1 region (using a glass electrode filled with 1 M NaCl and 10 mM 4-(2-hydroxyethyl)-1-piperazineethanesulfonic acid (HEPES), pH 7.4) and the stimuli were delivered to the Schaffer collateral pathway by a monopolar glass electrode filled with aCSF. fEPSP response was set to approximately 30% of the maximal fEPSP response i.e., approx. 0.2–0.3 mV, with stimulation intensity 10 μA ± 5 μA delivered via a stimulation box (ISO-Flex, A.M.P.I. Inc., Israel). Electrodes were placed superficially to maximize exposure to peptides. A stable baseline of 20 min bath application of aCSF under control conditions or with peptide was first obtained before induction for long-term plasticity recordings. The peptide was then also recirculated throughout the 1-h recording after induction. LTP was induced by high frequency stimulation: 2 × 100 Hz/1 s at 20 s interval. Sub-threshold LTD was induced by low frequency stimulation: 300 pulses at 1 Hz. On RjOrl:SWISS mice (3–6 weeks) slices, LTD was induced with low frequency stimulation: 900 pulses of 1 Hz in standard aCSF (see above) in presence of 50 μM picrotoxin (Sigma-Aldrich, dissolved in DMSO). On WT and APPdelETA mice (2–3 months), LTD was induced in a modified aCSF containing in mM: (in mM): 119 NaCl, 2.5 KCl, 1.25 NaH_2PO_4, 26 $NaHCO_3$, 2 $MgSO_4$, 4 $CaCl_2$ and 11 D-glucose, oxygenated with 95% O_2 and 5% CO_2, pH 7.4, without picrotoxin. MK801 (100 μM; Sigma-Aldrich, dissolved in DMSO) was used for some LTD experiments. For all LTD and LTP recordings, only the first third of the fEPSP slope was analyzed to avoid population spike contamination. The time courses were obtained by normalizing each experiment to the average value of all points constituting a 20 min stable baseline before induction. fEPSP magnitude was measured during the last 15 min of recording (45–60 min after induction) and calculated as % change fEPSP slope from baseline average. For analysis of LTD in APPdelETA mice in presence of L689,560, the drug was purchased from Tocris, prepared as a stock solution of 10 mM in DMSO and diluted to 10 μM (as recommended by[55] to avoid nonspecific effects) in aCSF on day of experiment. For PPRs, an EPSC at −65mV (naive slices from RjOrl:Swiss mice) or a fEPSP of ∼50% of the maximum (WT and APPdelETA mice) was obtained and two stimuli were delivered at 100, 200, or 300 ms inter-stimulus interval as indicated in figure. PPR was calculated as fEPSP2slope/fEPSP1slope (10 sweeps average per ISI). Recordings of control and peptide conditions were interleaved within the same day. Recordings of WT and APPdelETA mice were interleaved between days.

uEPSP and calcium transients in single spines

All procedures were carried out under local institutional guidelines, approved by the University of Bristol Animal Welfare and Ethical Review Board, and in accordance with the UK Animals (Scientific procedures) Act 1986. Transverse hippocampal slices from 4 to 5 week-old male C57/BL6J mice were used for simultaneous 2-photon imaging and current-clamp electrophysiology experiments. Dissection and slicing were performed in ice-cold sucrose based medium (in mM: 205 sucrose, 10 glucose, 26 $NaHCO_3$, 2.5 KCl, 1.25 NaH_2PO_4, 0.5 $CaCl_2$, 5 $MgSO_4$), 400 μm slices were then transferred to aCSF (in mM: 124 NaCl, 3 KCl, 26 $NaHCO_3$, 1.4 NaH_2PO_4, 10 Glucose, 1.3 MgSO4, 2.5 $CaCl_2$, 50 μM picrotoxin) saturated with 95% O_2 and 5% CO_2. Patch pipettes had resistances of 4–6 MOhm and were filled with a potassium-based intracellular solution containing: 150 K^+ methanesulfonate, 5 KCl, 10 HEPES, 3 MgATP, 0.4 Na_2GTP, with 20 μM Alexa Fluor 594 and 200 μM Fluo-4/5F. Spectra Physics Mai Tai pulsed lasers were tuned to 810 nm for imaging and 730 nm for uncaging. Image acquisition, uncaging and electrophysiological recordings were controlled using PrairieView (Bruker). Laser power at the slice surface was less than 10 mW. Pyramidal cells were visualized using Dodt gradient contrast and

Please cite this article in press as: Dunot et al., APP fragment controls both ionotropic and non-ionotropic signaling of NMDA receptors, Neuron (2024), https://doi.org/10.1016/j.neuron.2024.05.027

a 60× water immersion objective. Once whole-cell configuration was established, 2-photon excitation was used to visualize dendrites and spines (Alexa Fluo 594). Line scan images were acquired at least 30 min after breaking into the cell to allow for dye diffusion and equilibration. When the aCSF was supplemented with 2.5 mM MNI-caged-L-glutamate and 250 μM Trolox, the perfusion system was switched to a closed system. A series of five brief (1–2 ms) uncaging laser pulses targeted to a single spine was used to evoke EPSPs recorded using a Multiclamp 700B. Laser power, pulse duration and location were finely calibrated to elicit calcium transients only in the target spine as tested by line scans across neighboring spines and dendrites.[56] Electrophysiological signals were digitized at 20 kHz and low pass filtered at 4kHz. Membrane potentials were not corrected for the junction potential. Line scan series over 400 ms were acquired every 2–3 min. Plot profiles from individual line scan images were collected over the spine using ImageJ and the mean value for each time point quantified. The profile obtained from Fluo-4/5F (green ΔG) was divided by that obtained from Alexa 594 (red R), so $\Delta F = \Delta G/R$. $\Delta F/F$ values presented were obtained by dividing each ΔF by the 30 ms baseline before uncaging.

FLIM-FRET of GluN1-GFP/GluN1-mCherry FRET pair

Primary cultures of dissociated hippocampal neurons were prepared from E18 Sprague-Dawley rat embryos, as previously described.[57] Briefly, cells were plated at a density of 280×10^3 cells per dish on poly-L-lysine-coated Ø 18 mm glass coverslips kept in Ø 60 mm Petri dishes filled with Neurobasal medium supplemented with B-27 Plus (#A3653401, ThermoFisher Scientific, Waltham, MA, USA), GlutaMAX (#35050061, ThermoFisher Scientific), and 1.5% heat-inactivated horse serum. Cells were kept at 37°C/5% CO_2 and were transferred to serum-free medium after 3 days *in vitro* (div), half of which was replaced by fresh medium at 6 div. In order to perform FLIM-FRET measurements, 8–10 div cells were transfected with GluN1-GFP, GluN1-mCherry (gifts from Paul De Koninck),[21,51] and Flag-GluN2B (gift from R. Wenthold) at a ratio of 1:3:1 since we previously defined that this ratio provided optimal FRET signal.[19] The various plasmids were expressed in neurons using the calcium-phosphate co-precipitation method.[58] mCherry-GluN2B was expressed instead of GluN1-mCherry in a subset of cells as a negative control. After transfection, cells were transferred to BrainPhys medium (STEMCELL Technologies, #05790) supplemented with B-27 Plus and maintained at 37°C/5% CO_2 until the day of experimentation (13–15 div). Experiments were carried out at 37°C using an incubator box with an air heater system (Life Imaging Services, Switzerland) installed on an inverted Leica DMI6000B spinning disk microscope (Leica Microsystems, Germany) using the LIFA frequency domain lifetime attachment (Lambert Instruments BV, The Netherlands) and the LI-FLIM software. Cells were imaged with an HCX PL Apo CS 63X NA 1.4 oil-immersion objective using an appropriate filter set. GFP fluorescence was excited using a sinusoidally modulated 3 W/478 nm LED at 36 MHz under wild-field illumination. Emission was collected using an intensified CCD LI2CAM camera (Lambert Instruments BV). Acquisitions were performed after a 10 min incubation with either synthetic AETA or CtrlP peptides (10 nM). The experimenter was blind to the conditions until final analysis. Lifetimes were calibrated using a reference solution of erythrosin B (1 mg/mL) with an average lifetime of 0.086 ns. The lifetime of the sample was determined from the fluorescence phase-shift between the sample and the reference from a set of 12 phase settings using the LI-FLIM software provided by the manufacturer. GFP fluorescence lifetimes were measured in dendritic spine clusters defined by the user based on confocal images of the fluorescence signals of the donor (GluN1-GFP) and acceptor (GluN1-mCherry) fluorophores, blind to the FLIM image. For each neuron, a total of 20–30 dendritic spines clusters were selected, from which lifetime values were extracted using the LI-FLIM software. FRET efficiencies were calculated—either from a random selection of cluster lifetime values or from mean lifetime values per neuron—for each experimental condition using the following equation:

$$FRET\ efficiency\ (\%) = \frac{(\tau D - \tau DA) * 100}{\tau D}$$

where τD is the GFP fluorescence lifetime when the FRET donor (GluN1-GFP) is expressed alone, and τDA is the GFP fluorescence lifetime when the FRET donor is expressed together with the acceptor (GluN1-mCherry).[51]

Two-photon imaging of spine structural plasticity

Acute hippocampal slices were prepared from P18-P21 GFP-M mice[59] of both sexes, as described.[13] All experimental protocols were approved by the University of California Davis Institutional Animal Care and Use Committee. GFP-expressing CA1 pyramidal neurons were imaged using a custom two-photon microscope.[60] For each neuron, image stacks (512 × 512 pixels; 0.02 μm per pixel; 1-μm z-steps) were collected from a tertiary basal dendrite at 5 min intervals at 30°C in recirculating artificial cerebral spinal fluid (aCSF; in mM: 127 NaCl, 25 $NaHCO_3$, 1.2 NaH_2PO_4, 2.5 KCl, 25 D-glucose, aerated with 95%O_2/5%CO_2, ~310 mOsm, pH 7.2) with 2 mM Ca^{2+}, 0.1 mM Mg^{2+}, and 1 μM TTX. Slices were pre-incubated for 20 min with CtrlP or AETA. Images are maximum projections of image stacks after applying a median filter (2 × 2) to raw image data. Estimated spine volume was measured from background-subtracted green fluorescence using the integrated pixel intensity of a boxed region surrounding the spine head, as described.[60] High-frequency uncaging (HFU) consisted of 60 pulses (720 nm; 2 ms duration, ~12 mW at the sample) at 2 Hz delivered in ACSF containing (in mM): 2 Ca^{2+}, 0.1 Mg^{2+}, 0.001 TTX, and 2.5 MNI-glutamate. The beam was parked at a point 0.5–1 μm from the spine at the position farthest from the dendrite. Cells for each condition were obtained from 6 independent hippocampal acute slices preparations of both sexes. Data collection and analysis was done blind to the experimental condition. All statistics were calculated across cells. two-way ANOVA with Bonferroni's multiple comparisons was used.

BACE1 inhibition *in vivo*

To increase endogenous AETA levels, 6 weeks old male RjOrl:SWISS mice (Janvier, France) were administered the BACE1 inhibitor LY2811376 (100 mg/kg) by oral gavage.[25] LY2811376 was obtained from Medchem Express (Sweden) and prepared in 10% DMSO, 40% PEG300, 5% Tween-80, and 45% saline. After slicing and recovery (1h at 37°C), slices were incubated in LY2811376 (5 μM) throughout experiment. NMDAR sEPSC and LTD recordings were performed as described above.

In vivo neuronal activation or inhibition by DREADD

The procedure was performed essentially as described previously[61] in accordance with the recommendations of the European Commission (2010/63/EU) for care and use of laboratory animals and approved by the French National Ethical Committee (#16459–2018061116303066). AAV8-hSyn-hM3Dq-mCherry (#50474) and AAV8-hSyn-hM4Di-mCherry (#50475) were purchased from Addgene and injected in pre-frontal cortex by stereotaxic surgery in 8 week-old male C57/BL6J mice (Janvier Labs, France). Stereotaxic injections were performed using a stereotaxic frame (Kopf Instruments). General anesthesia was achieved using a mix of ketamine (150 mg/kg) and xylazine (10 mg/kg). Viruses were injected bilaterally at a rate of 100 nL/min for a final volume of 500 nL per site. Stereotaxic coordinates were (in mm): antero-posterior (AP): +1,7; Mediolateral (ML): +/− 1,5; dorsoventral (DV): −1,5; based on the Paxinos atlas of the adult mouse brain. Coordinates were taken from bregma for AP and ML coordinates, and from skull at the site of injection for DV. Mice were given a 3-week-recovery period to allow sufficient viral expression. CNO (1 mg/kg, Sigma-Aldrich, France) or saline (0.9% NaCl, 10 mL/kg) was administered by intraperitoneal injection 30 min before microdissection of transduced tissue. Brains were then removed, mCherry-positive tissues were visualized with a DFP-1 duel fluorescence protein flashlight (NIGHTSEA, USA) and dissected out to be snap-frozen in liquid nitrogen for immunoblotting (see immunoblotting section). A subgroup of slices with transduced virus were mounted and visualized under a Vectra 3 (PerkinElmer) microscope to assess virus spread.

Generation of APPdelETA mice

APPdelETA mice were generated by CRISPR/Cas9-assisted gene editing in zygotes as described previously.[62] Briefly, pronuclear stage zygotes were obtained by mating C57BL/6J males with superovulated C57BL/6J females (Charles River, Germany). Embryos were then microinjected into the male pronucleus with an injection mix containing APP-specific CRISPR/Cas9 ribonucleoprotein (RNP) complexes. RNPs consisted of 50 ng/μL Cas9 protein (IDT, Coralville, USA), 1 μM crRNA APP-Ex12up (protospacer GAACTACTCCGACGATGTCT; IDT), 1 μM crRNA APP-Ex12dn (protospacer CGCTCTCATGCCTTCGCTGA; IDT), and 1 μM tracrRNA (IDT, Coralville, USA). After microinjection, zygotes were cultured in KSOM medium until transferred into pseudo-pregnant CD-1 foster animals. A mutant founder carrying a 123 bp deletion was crossed to a C57BL/6J animal to establish the stable APPdelETA line. All mice were handled according to institutional guidelines approved by the animal welfare and use committee of the government of Upper Bavaria and housed in standard cages in a specific pathogen-free facility on a 12-h light/dark cycle with *ad libitum* access to food and water. To identify putative off target sites of the APP-specific crRNAs, the CRISPOR online tool[63] was used. TOP12 predicted sites (combined CFD and MIT score) were chosen for off-target analysis. For analysis, genomic DNA of wildtype and heterozygous mutant F1 APPdelETA mice was isolated and predicted loci were PCR amplified with primers flanking the putative cut sites and subsequently Sanger sequenced using the PCR primers. No off-target events were detected. Genotyping of the line is performed with this set of primers in a standard PCR reaction from tail biopsies: APPintron11-12for (AAGCTCTGACTTTCCTTAAGGTGC) and APPintron12-13rev (TAGGAGTGGTATCCCTGCGGGT). The PCR products are cleaved with the restriction enzyme Bcl1 (New England Biolabs, Germany) with no cleavage for the KI/KI (510 bp) and two bands for the WT allele resulting products of 318 bp and 192 bp. To quantify AETA and CTF-η levels, hippocampi of APPdelETA mice and WT littermates were dissected out, snap frozen in liquid nitrogen and kept in −80°C freezer until processed for immunoblotting.

Generation of AETA-m mouse line

AETA-overexpressing mice (Thy-1.2-Aη-α; AETA-m) were generated using C57Bl6/NCrl Donor mice mated by superovulation (46 h between pregnant mare serum gonadotropin (PMSG) and human chorionic gonadotropin (HCG)) at the midpoint of the dark period (12 h/12 h, 6 a.m. to 6 p.m. light circle). After positive plug detection in the morning, the cumulus complexes were isolated and zygotes removed with a treatment of hyaluronidase (Sigma-Aldrich; final concentration of 0.1% (801 U/ml)). Transgenic mice were back-crossed on C57Bl6/J. The linearized Thy1.2 cassette coding for a secreted version of human AETA DNA plasmid was injected into the male pronucleus of fertilized zygotes by using a motor driven manipulator-based microinjection stage. About 2 h after injections, the surviving embryos were transferred into Crl:CD1(ICR) pseudopregnant recipient female mice (ca. 20 embryos per recipient). The recipient mice were mated with sterile males (vasectomized) Crl:CD1(ICR). By detection of a copulation plug in the morning of the transfer day, pseudopregnant mice can be used for the unilateral surgical embryo transfer procedure into the oviduct. Anesthesia was induced by intraperitoneal (i.p.) injection with a mix of Ketamin/Xylazin and Acepromazine. Mice were generated under the license 24-9168.11-9/2012-5. All animal experiments were performed in accordance with the European Communities Council Directive (86/609/EEC), and were approved by the local ethics committee (Government of Saxony, Germany). Immunoblotting of rodent AETA levels and human AETA levels was performed as described below. Levels of A$\beta_{1\text{-}40}$ was quantified using the Wako Human/Rat (Mouse) β-Amyloid (40) ELISA Kit (Catalog Number: 294–62501) as per manufacturer's instructions.

Immunoblotting

The brain homogenates for the analysis of APP processing products (APP-FL, CTF-η, AETA) were essentially prepared as described previously.[16] In brief, DEA lysates (0.2% Diethylamine in 50 mM NaCl, pH 10) and RIPA lysates (20 mM Tris-HCl pH 7.4, 150 mM NaCl, 1 mM Na_2EDTA, 1% NP-40, 0.5% sodium deoxycholate, 0.05% Triton X-100) with protease inhibitors (Sigma-Aldrich, P8340) were prepared from brain samples using the Precellys system (Bertin) for homogenisation followed by ultracentrifugation. For the DEA and RIPA samples we used the Bradford (Biorad) to measure the protein concentration, which was adjusted equally to all samples before Western blot analysis. For detection by Western blotting, proteins were separated on 8–12% Tris-Glycine gels or alternatively on Tris-Tricine (10–20%, Thermo Fisher Scientific) gels, transferred to nitrocellulose membranes (0.1 μm, GE Healthcare) which were boiled for 5 min in PBS and subsequently incubated with the blocking solution containing 0.2% I-Block (Thermo Fisher Scientific) and 0.1% Tween 20 (Merck) in PBS for 1 h, followed by overnight incubation with 2 μg/mL antibody in the blocking solution. Antibody detection was performed using the corresponding anti-rat/mouse/rabbit-IgG-HRP conjugated secondary antibody (Thermo Fisher Scientific) and chemiluminescence detection reagent ECL (Thermo Fisher Scientific). Antibodies used for immunoblotting are M3.2 (Biolegend, #805701; mouse IgG) for detection of mouse AETA, antibodies 2D8 and 2E9 for human AETA,[16] 22C11 (Merck, #MAB348; mouse IgG) for APP-FL, Y188 (abcam, #32136; rabbit IgG) for CTF-η, a polyclonal serum for mCherry (Takara, # 632496, rabbit IgG), Synaptophysin (Sigma-Aldrich, S5786, mouse IgG) and Synaptobrevin-2 (SYSY, #104211, mouse IgG), p-38 (#8690, Cell Signaling, rabbit IgG), p-p38 (#9216, Cell Signaling, mouse IgG). For the loading control, when necessary, we used an antibody specific to β-actin (Sigma-Aldrich, #AC-74). AETA was quantified in DEA fraction and CTF-η was quantified in RIPA fraction. For analysis of APPdelETA and WT mouse tissue, peptide levels were normalized to β-actin or ponceau (as stated in results description), and normalized to WT average for each immunoblot for statistical analysis (Mann-Whitney test) using GraphPrism 8. For DREADD experiment, AETA levels and mCherry levels were normalized to β-actin. AETA levels were further normalized to mCherry levels. Outliers in values obtained for AETA/mCherry ratio (1 hM3D-SAL and 1 hM4D-CNO) were not considered for statistical analysis (see Figure S4). Ratios were further normalized to average Saline of each experiment to pool all experiments together and perform statistical analysis (Mann-Whitney test).

Golgi-Cox staining for spine density analysis

Brains of WT and APPdelETA mice were collected and processed for Golgi-Cox impregnation. Brains were removed and impregnated in a Golgi-Cox solution (1% potassium dichromate, 1% mercuric chloride, 0.8% potassium chromate) for 3 weeks at room temperature according to manufacturer instruction (FD rapid GolgiStain kit, FD Neurotechnologies, USA). Brains were sectioned coronally (80 μm) using a vibratome and stained and mounted according to protocol. Images were acquired under white light on a DMD108 Leica microscope (×60 magnification). Spine density (number of spines per 1 μm length) in selected segments (minimum of 30 per mouse) of secondary dendrites of CA1 pyramidal neurons in stratum radiatum was estimated using ImageJ and manual count.

Contextual fear conditioning

Behavioral analysis was performed in accordance with the European directives 2010/63/EU on the Protection of Animals used for Scientific Purposes in the framework of project authorizations APAFIS#6856–2016091610462338 and APAFIS#37493–2022050311352580 as delivered by the competent French authorities. All animals were daily handled for 2 min during one week. To measure electric shock-induced freezing, each mouse was placed individually in a soundproof test chamber containing a floor made of a grid with 27 stainless-steel rods (diameter 4 mm) spaced 1 cm apart and connected to a generator to allow shock delivery (Shocker LE 100-26 Panlab Harvard Apparatus Bioseb). Mice were left to freely explore the apparatus for 3 min and then received three consecutive electrical foot shocks (intensity: 0.7 mA, duration: 2 s) with a 1 min interval between each shock. Mice remained in the test chamber 1 min after the last foot shock. Activity levels of mice were recorded through a high-precision sensor plate placed beneath the floor grid (Load cell coupler LE 111 Panlab Harvard Apparatus Bioseb) to assess the variations of weight induced by the movements of the mice. To test for aversive memory formation, mice were re-exposed 24 h after to the same context for 6 min without any shock. Freezing was defined as total lack of movement aside from breathing for a cumulative duration of at least 2s. The freezing behavior was scored using high-precision sensor plate.

Statistical analysis

Results are shown as mean ± s.e.m. Numbers and their correspondence are given in each figure. Statistical analysis was performed with GraphPrism software. Statistical analyses are described in brief in figure legends and are presented in detail in the supplemental statistics (Data S1). Statistical significance was set at $p < 0.05$: *$p < 0.05$; **$p < 0.01$; ***$p < 0.001$; ****$p < 0.0001$.

Neuron, Volume *112*

Supplemental information

APP fragment controls both ionotropic and non-ionotropic signaling of NMDA receptors

Jade Dunot, Sebastien Moreno, Carine Gandin, Paula A. Pousinha, Mascia Amici, Julien Dupuis, Margarita Anisimova, Alex Winschel, Magalie Uriot, Samuel J. Petshow, Maria Mensch, Ingrid Bethus, Camilla Giudici, Heike Hampel, Benedikt Wefers, Wolfgang Wurst, Ronald Naumann, Michael C. Ashby, Bodo Laube, Karen Zito, Jack R. Mellor, Laurent Groc, Michael Willem, and Hélène Marie

Supplemental information

APP fragment controls both ionotropic and non-ionotropic signaling of NMDA receptors.

Jade Dunot, Sebastien Moreno, Carine Gandin, Paula A. Pousinha, Mascia Amici, Julien Dupuis, Margarita Anisimova, Alex Winschel, Magalie Uriot, Samuel J Petshow, Maria Mensch, Ingrid Bethus, Camilla Giudici, Heike Hampel, Benedikt Wefers, Wolfgang Wurst, Ronald Naumann, Michael C. Ashby, Bodo Laube, Karen Zito, Jack R. Mellor, Laurent Groc, Michael Willem and Hélène Marie

Figures S1-S15

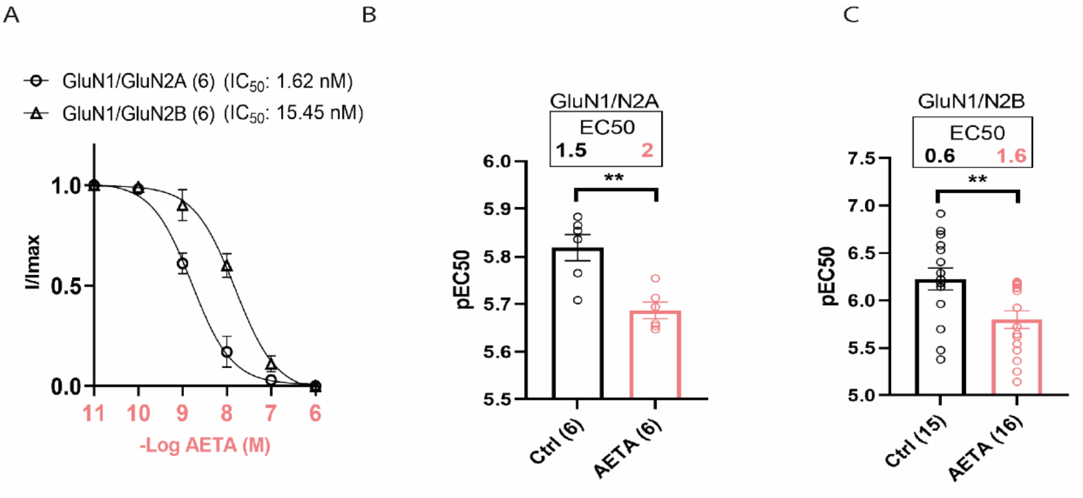

Figure S1 (related to Figure 1) AETA inhibits recombinant GluN1/GluN2A and GluN1/GluN2B NMDARs in oocytes by competing with glycine.

(A) AETA inhibition curves for GluN1/GluN2A and GluN1/GluN2B, from which the respective IC_{50} of AETA inhibition were calculated. Data represent mean ± s.e.m. n = 6 independent oocytes per condition. **(B-C)** pEC_{50} values and EC_{50} were calculated from dose-response activation curves for glycine (Figure 1I) for GluN1/GluN2A (B) and GluN1/GluN2B (C). n= oocytes per condition. See supplemental statistics (*Data S1*) for full statistics.

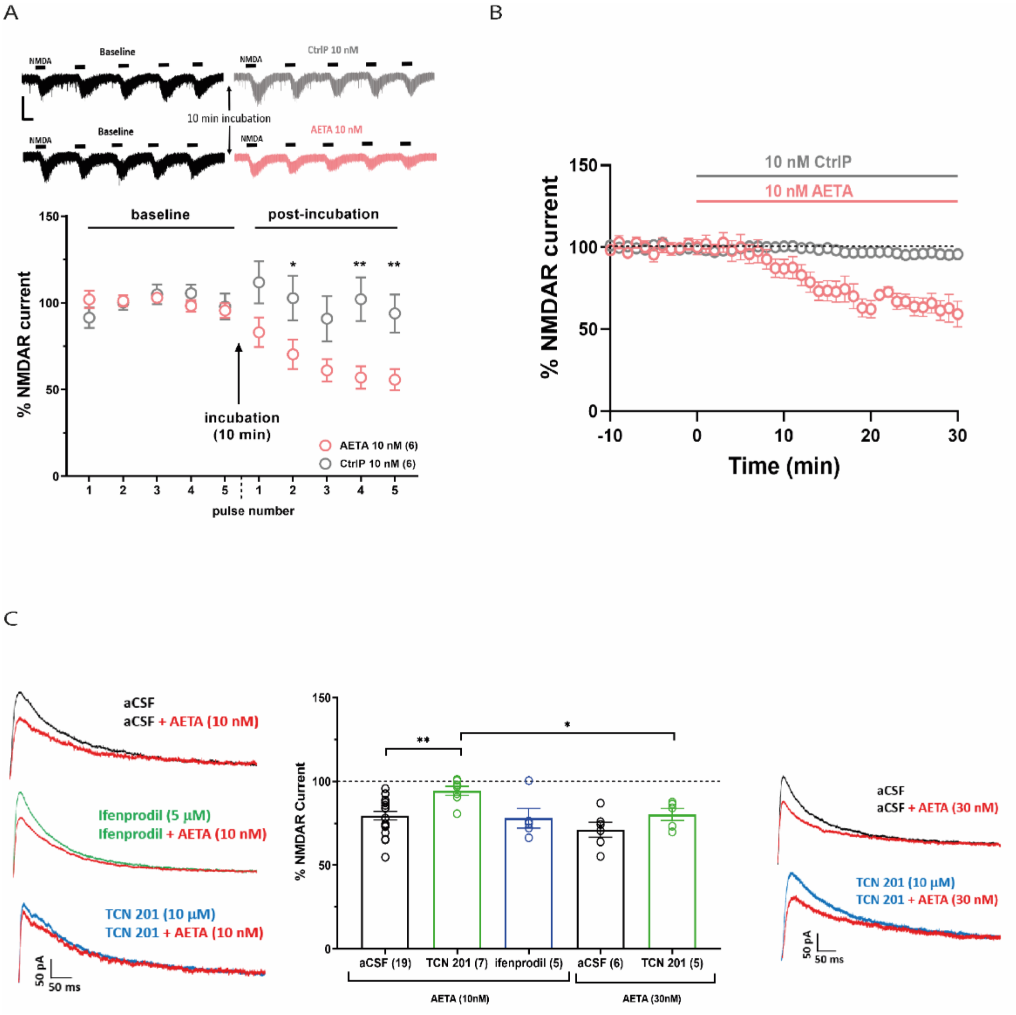

Figure S2 (related to Figure 1) AETA inhibits native NMDAR current in cultured hippocampal neurons and adult CA1 pyramidal neurons exhibiting a stronger inhibition for GluN2A containing NMDARs. (A) (Top) Representative traces of NMDAR current elicited in cultured neurons in response to 5 applications of NMDA (30 μM/10 s) before (baseline) and 10 minutes after incubation with 10nM of CtrlP or AETA; scale bars: 10 s/100 pA. (Bottom) Graph represents time course of % peak current (normalized to baseline average of the 5 pulses) of recordings as shown in top. n= 6 neurons per condition. **(B)** Time course of % NMDAR current (normalized to averaged baseline) recorded at CA3-CA1 synapse of adult mouse slices upon application of 10 nM CtrP or AETA (Data quantified and shown in Figure 1C). **(C)** (Left, Right) Representative traces and (middle) Bar graph of % NMDAR current (normalized to averaged baseline) recorded at CA3-CA1 synapse of adult mouse slices before (baseline) and after application of AETA (10 nM) or (30 nM) in aCSF or aCSF containing GluN2A current inhibitor TCN 201 (10 μM) or aCSF containing GluN2B current inhibitor ifenprodil (5 μM). 10 nM AETA still had an effect in presence of ifenprodil (blockage of GluN2B). While 10 nM AETA did not have any effect in presence of TCN 201 (blockage of GluN2A), 30 nM AETA still partially inhibited the TCN 201-insensitive current. See supplemental statistics (*Data S1*) for full statistics.

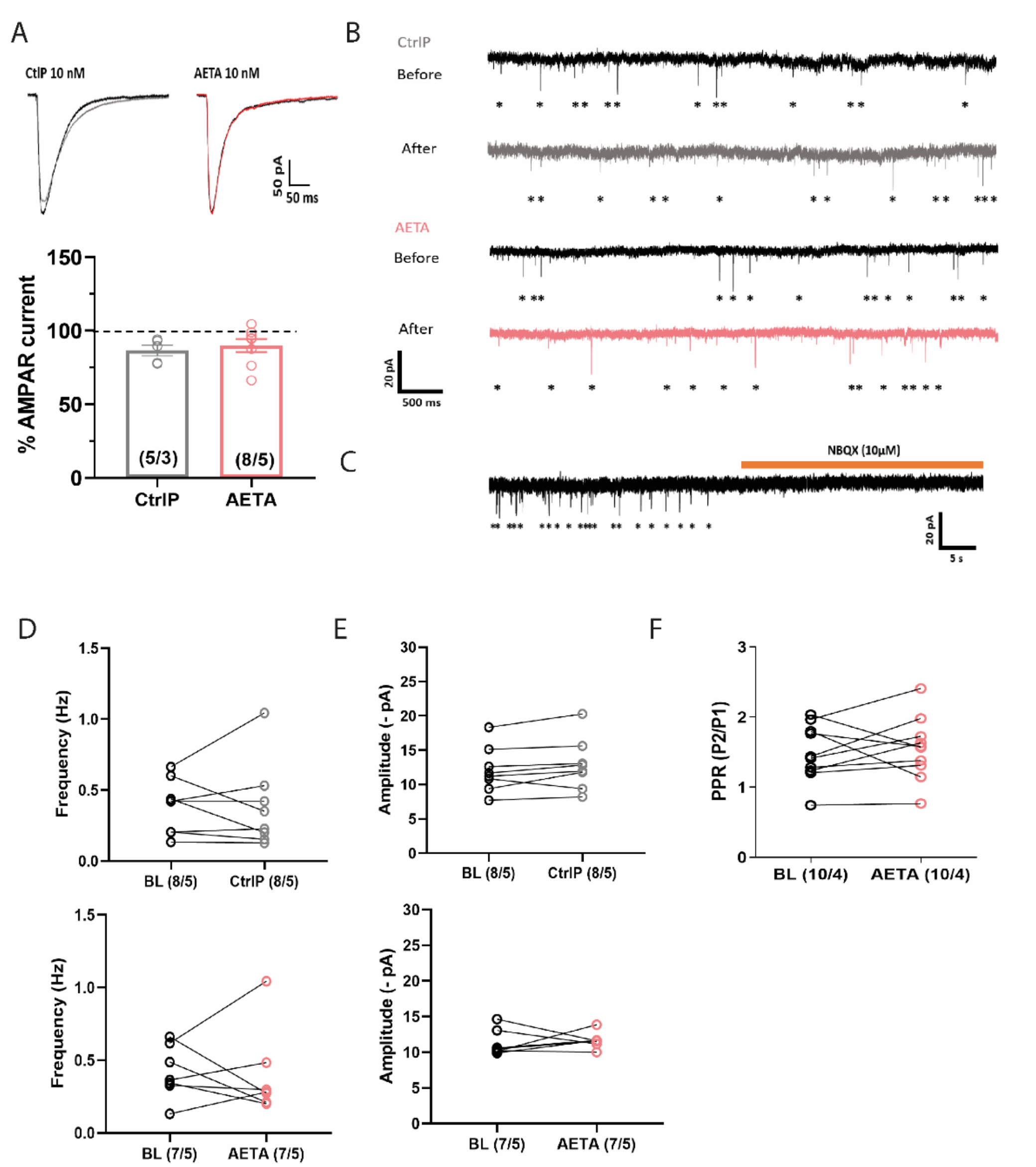

Figure S3 (related to Figure 1) - AETA does not impact native synaptic AMPAR currents nor short term pre-synaptic plasticity.

(A) Bar graph of evoked AMPAR current peak amplitude at CA3-CA1 synapse in mouse hippocampal slices 25-30 min post application of either AETA (10 nM) or CtrlP (10 nM). **(B)** Representative traces of AMPAR sEPSCs before and after application of CtrlP (top) or AETA (bottom) (10 nM). **(C)** Representative recorded trace of AMPAR sEPSCs (stars) that disappear upon application of AMPAR blocker NBQX. **(D)** AMPAR sEPSC frequency and **(E)** amplitude calculated before (baseline, BL) and after bath application of CtrlP (top) or AETA (bottom) (10nM). **(F)** Paired-pulse ratio (100 ms inter-stimulus interval) measured before (baseline, BL) and after (10 min) application of AETA (50 nM) at CA3-CA1 synapse in mouse hippocampal slices. (n/N= neuron/mice). See supplemental statistics (*Data S1*) for full statistics.

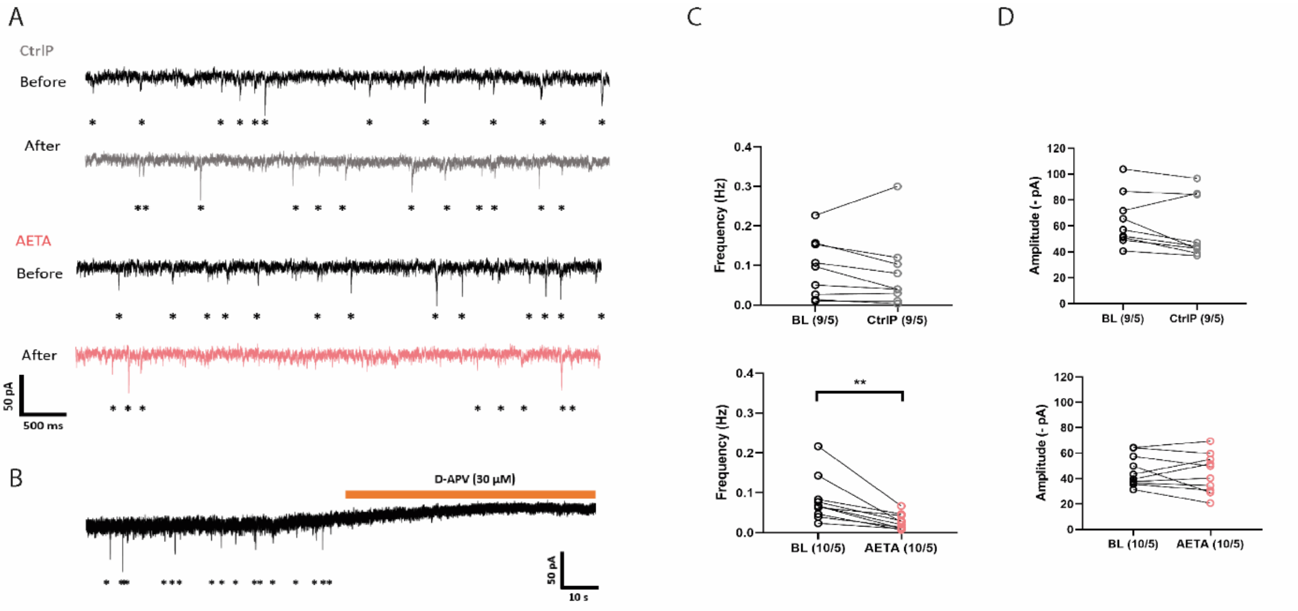

Figure S4 (related to Figure 1) – AETA modifies spontaneous NMDAR EPSCs frequency but not amplitude.

(A) Representative traces of NMDAR sEPSC before and after application of CtrlP (top) or AETA (bottom) (10 nM). **(B)** Representative recorded trace of NMDAR sEPSCs (stars) that disappear upon application of NMDAR blocker D-APV. Note also the shift in tonic current that represents blockage of tonically activated NMDARs. **(C)** NMDAR sEPSC frequency and **(D)** Amplitude calculated before (baseline, BL) and after (10 min) bath application of AETA or CtrlP (10 nM). See supplemental statistics (*Data S1*) for full statistics.

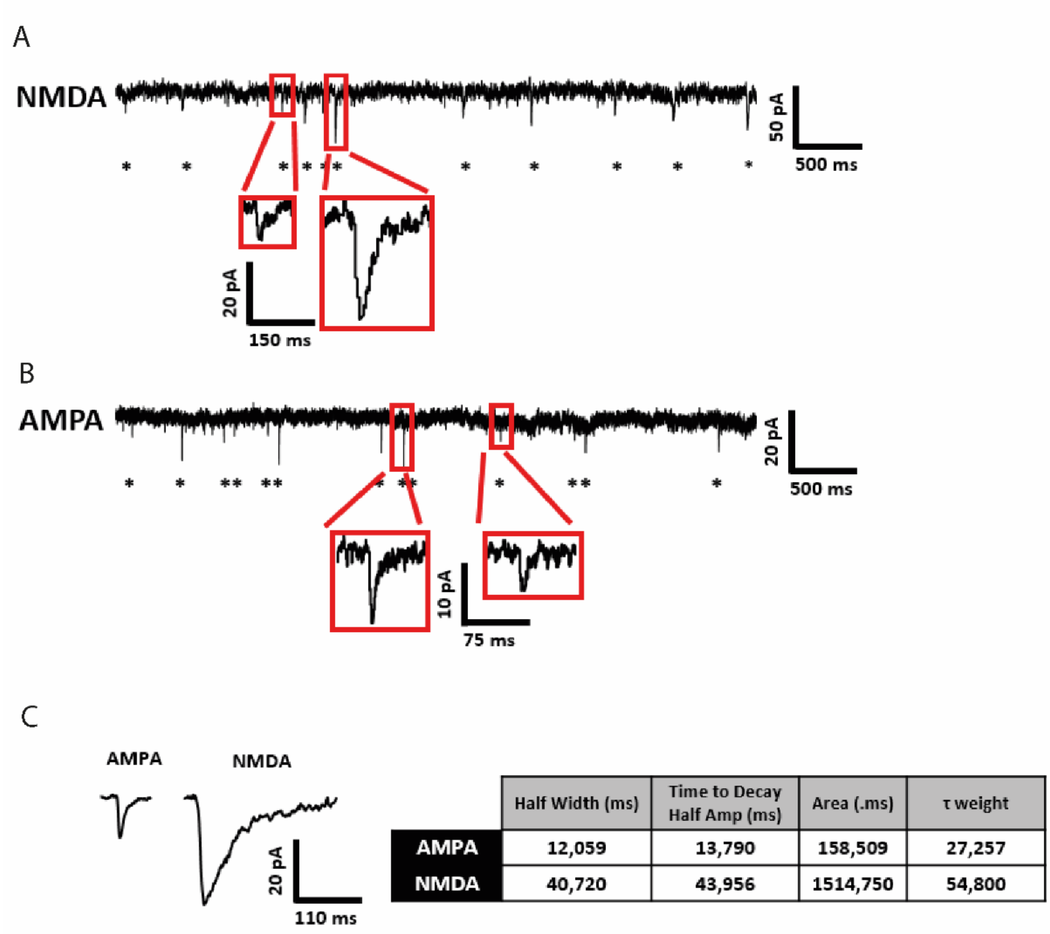

	Half Width (ms)	Time to Decay Half Amp (ms)	Area (.ms)	τ weight
AMPA	12,059	13,790	158,509	27,257
NMDA	40,720	43,956	1514,750	54,800

Figure S5 (related to Figure 1) : Kinetics of AMPAR and NMDAR EPSCs.

(A) representative trace of NMDAR EPSCs with zoom windows on small and large EPSCs. (B); representative trace of AMPAR EPSCs with zoom windows on small and large EPSCs. (C): Representative averaged (20 traces) AMPAR and NMDAR EPSCs with their kinetic values.

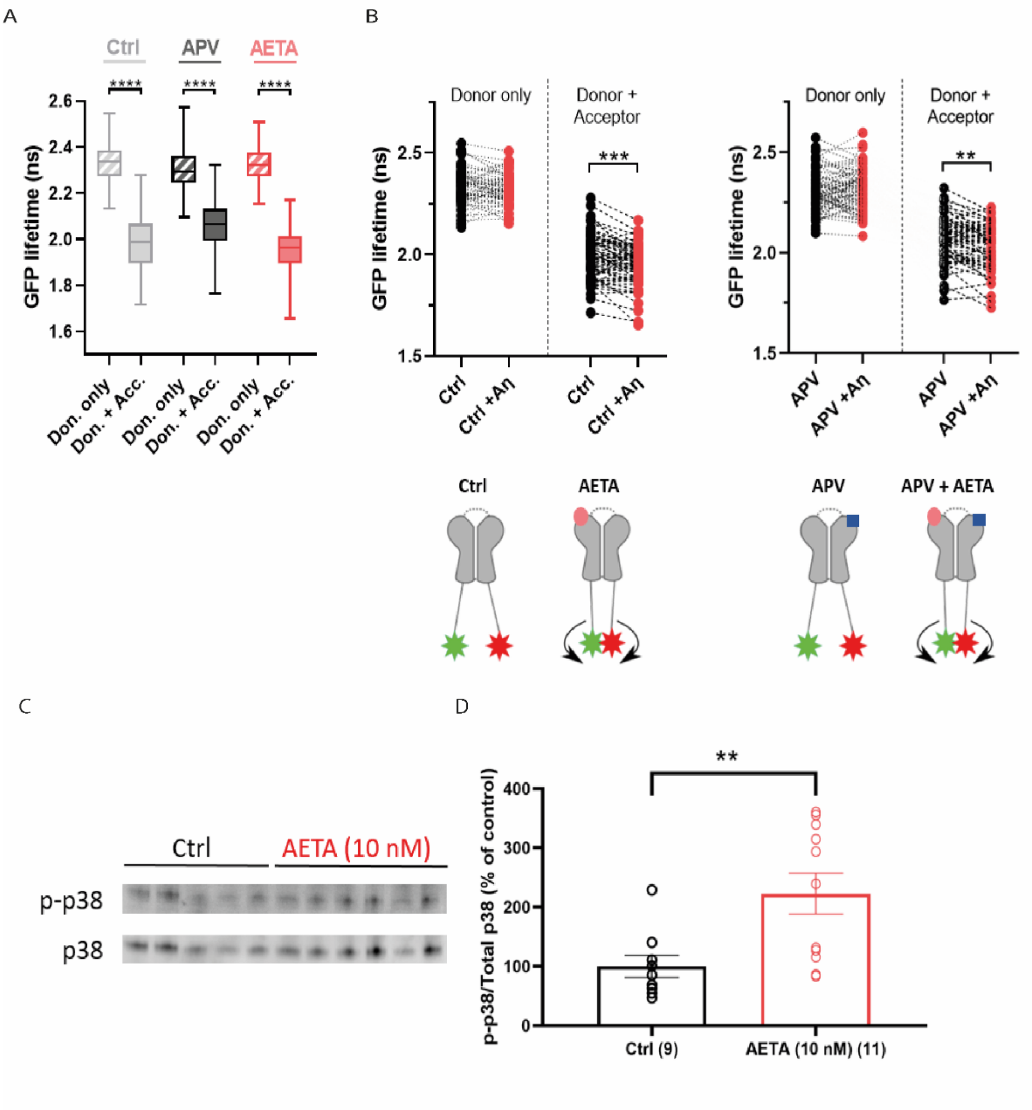

Figure S6 (related to Figure 2) : AETA still modifies NMDAR conformation in presence of NMDAR competitive antagonist APV and increases p38 phosphorylation.

(A) Graph represents GFP lifetime in GluN1-GFP only (Don. only) and GluN1-GFP/GluN1-mCherry (Don. + Acc.) clusters 10 min after exposure to Ctrl (Tyrode) (Don. Only, n = 62 clusters; Don. + Acc., n = 69 clusters) or APV (50µM; Don. Only, n = 74 clusters; Don. + Acc., n = 65 clusters) or AETA (10 nM; Don. Only, n = 62 clusters; Don. + Acc., n = 69 clusters) **(B)** Graph represents GFP lifetime in GluN1-GFP and GluN1-GFP /GluN1-mCherry clusters 10 min after exposure to Ctrl (Tyrode; Don. only n = 62; Don. + Acc. n = 79) or APV (50µM; Don. only n = 79; Don. + Acc. n = 65) then 10 min after exposure to AETA (10 nM). *Bottom*, Illustration of movement of GluN1 intracellular tail in basal condition (Ctrl or APV) and in presence of AETA. **(C)** Example immunoblotting of phosphorylated p38 (p-p38) and p38 (same gel) of neuron culture lysates in control (Ctrl) or after 20 min of incubation with AETA (10 nM). The analysis was performed in duplicate. Full blots are provided in additional supplementary material (Data S2). **(D)** Ratio of p-p38 on total p38 obtained from immunoblots shown in (C). n= number of independent samples. Statistics: (A) paired t-test and Mann Whitney; (B) paired t-test and Wilcoxon test; (D) Mann Whitney test (D). See supplemental statistics (*Data S1*) for full statistics.

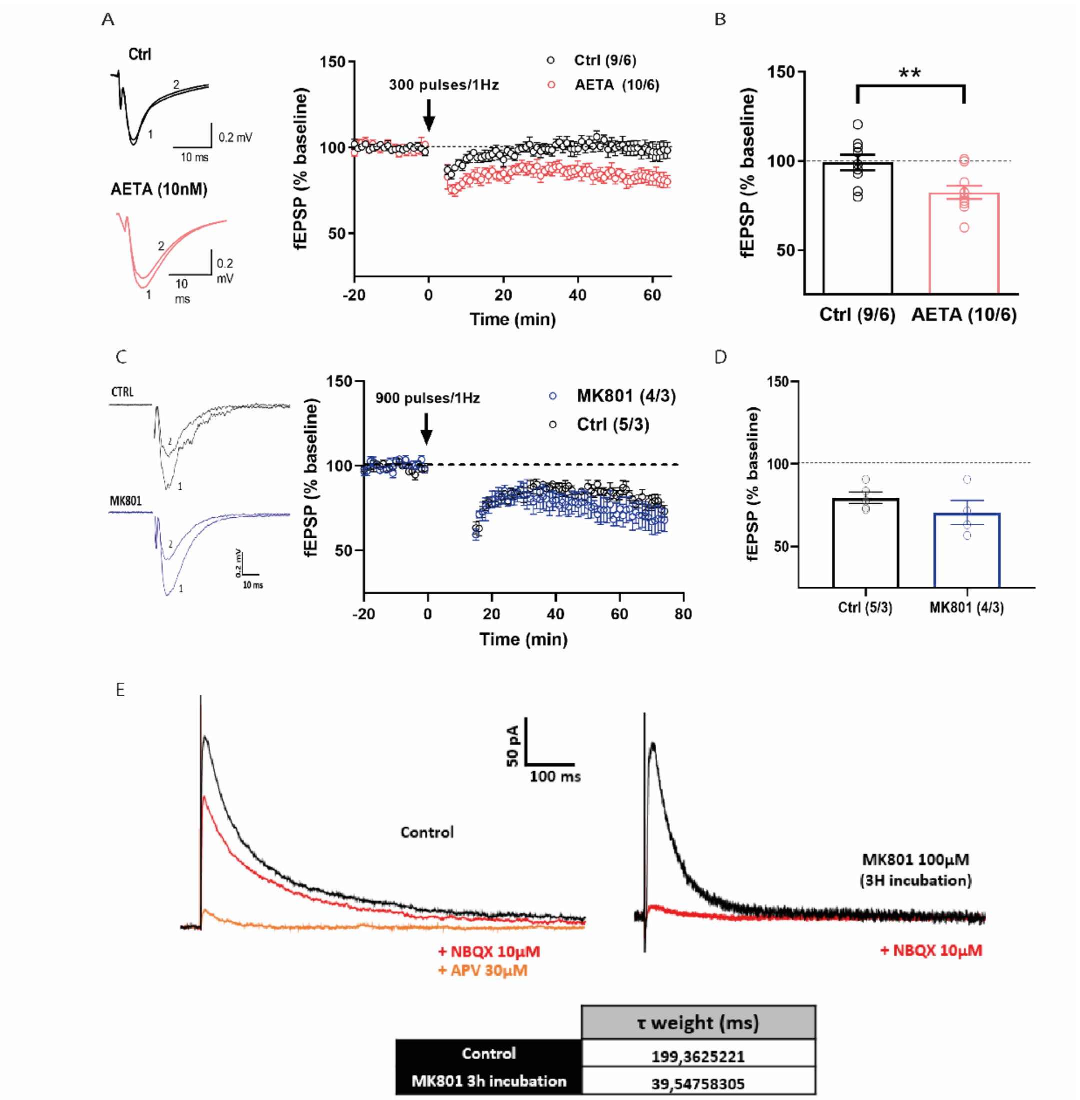

	τ weight (ms)
Control	199,3625221
MK801 3h incubation	39,54758305

Figure S7 (related to Figure 2) – LTD is induced by sub-threshold protocol in presence of AETA and MK801-independent LTD is observed at CA3-CA1 synapse in rat hippocampal slices.
(A) Summary graph (right) of fEPSP slope (% baseline) pre- and post-subLTD induction (time 0) in control (Ctrl, aCSF only) or in presence of AETA (10 nM) throughout recording. **(B)** Summary of fEPSP magnitude 45-60 min after subLTD induction as fEPSP (% baseline) for data shown in (A). **(C)** Summary graph of fEPSP slope (% baseline) pre- and post-LTD induction (time 0) in control (Ctrl, aCSF only) or after 3h of pre-incubation with MK801 (100 µM, also present in recording bath) recorded at CA3-CA1 synapse in rat hippocampal slices. **(D)** Summary of fEPSP magnitude 45-60 min after LTD induction as fEPSP (% baseline) for data shown in (C). **(E)** Representative trace of EPSC recorded in control (black), after NBQX (red) and APV (orange) without (left) or after 3 hours of preincubation of slice in MK801. The NMDAR-dependent current, normally observed under NBQX (red trace on left recording) is completely absent after MK801 preincubation (red trace on right recording). τ weight value is also shown for the two black traces showing loss of slow current after MK801 incubation. Statistics: Two-tailed unpaired Student’s t-test (B and D). See supplemental statistics (*Data S1*) for full statistics.

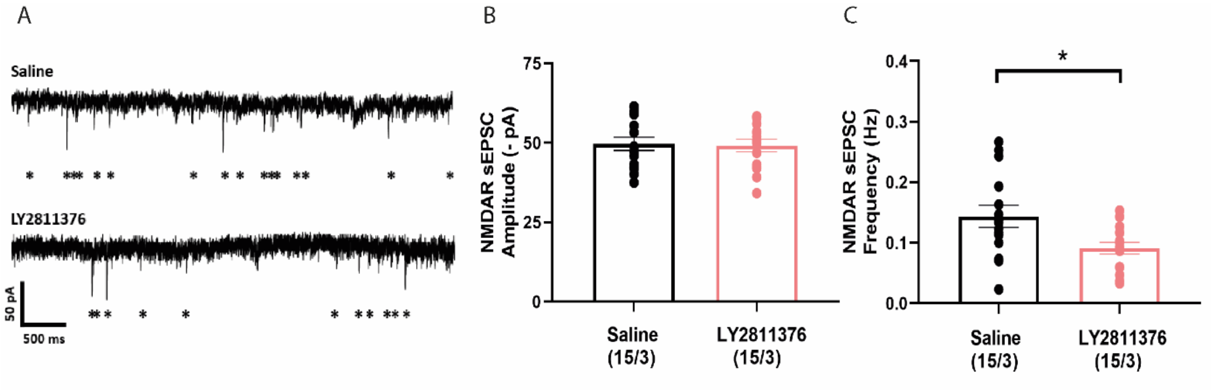

Figure S8 (related to Figure 3) : Endogenous increase of AETA by *in vivo* BACE-1 inhibition leads to decreased NMDAR EPSC frequency.

(A) Representative traces of NMDAR sEPSCs recorded in CA1 pyramidal of hippocampal slices from saline and LY2811376 treated mice. **(B)** NMDAR sEPSC frequency and **(C)** Amplitude calculated from traces as shown in (A). n/N= neurons/mice. See supplemental statistics (*Data S1*) for full statistics.

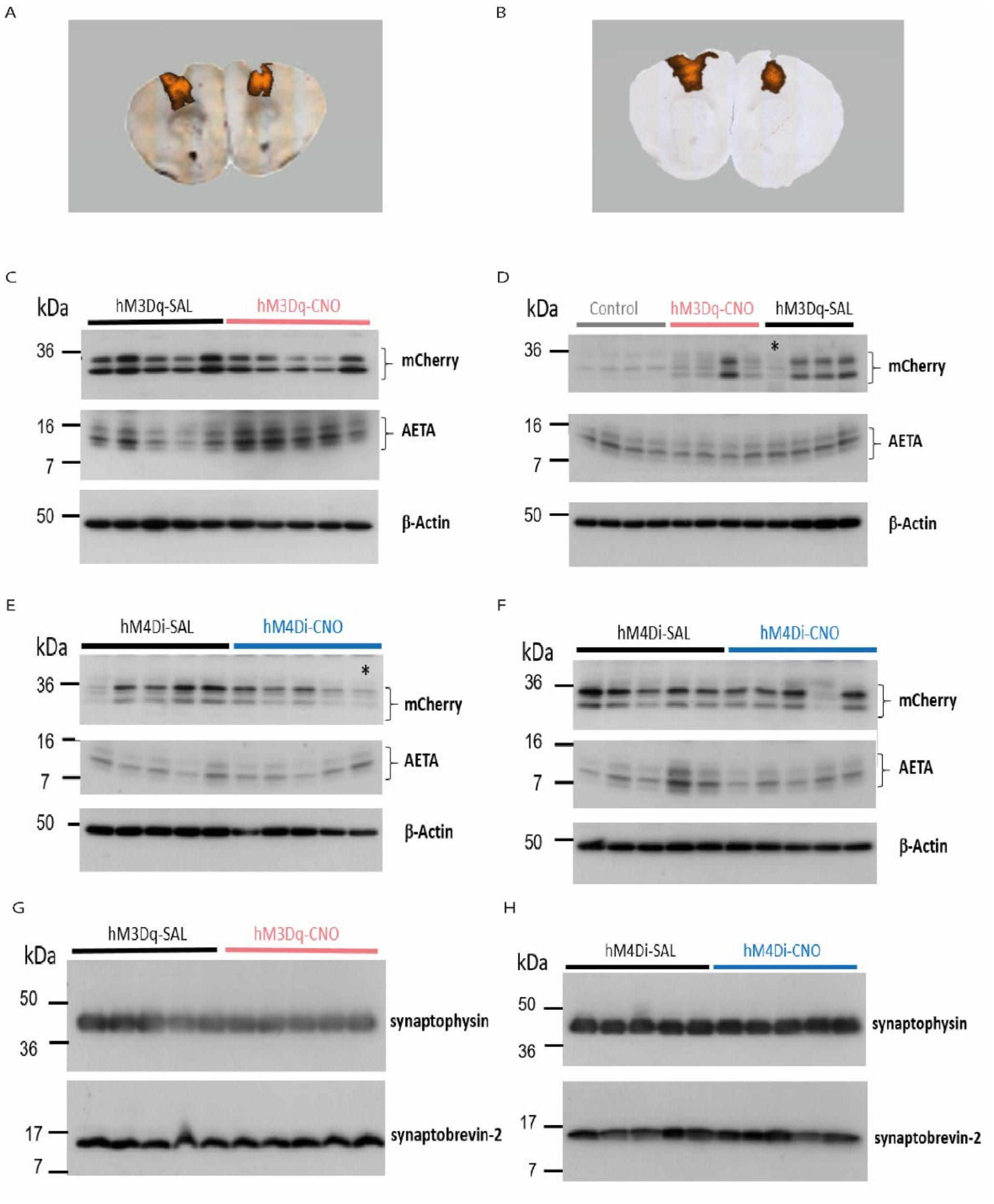

Figure S9 (related to Figure 3) – *In vivo* viral expression of hM3Dq-mCherry and hM4Di-mCherry and blots for quantification of AETA and synaptic proteins in hM3Dq and hM4Di transduced tissues.
(A) Representative image of AAV-hM3Dq-mCherry transduction in the prefrontal cortex (PFC). (**B**) Representative image of AAV-hM4Di-mCherry transduction in the PFC. (**C-D**) 18 mice were transduced with AAV-hM3Dq-mCherry and were injected i.p. with saline (9 mice) or CNO (9 mice). 30 min post injection, mCherry fluorescent tissues (both PFC injection area per mouse) were collected and processed for immunoblotting for AETA, mCherry and β-actin. 4 control PFC samples were also processed and blotted to check for specificity of mCherry antibody. **(E-F)** Same experiment as in (C-D) but for 20 mice transduced with AAV-hM4Di-mCherry (10 saline and 10 CNO). (**G-H**) overall health of infected tissue for each viral transduction was confirmed by reblotting some of the membranes with two synaptic markers: synaptophysin and synaptobrevin-2. * denotes two samples that were excluded from statistical analysis because AETA/mCherry ratios were detected as outliers in GraphPrism. Full blots are provided in additional supplementary material (Data S2).

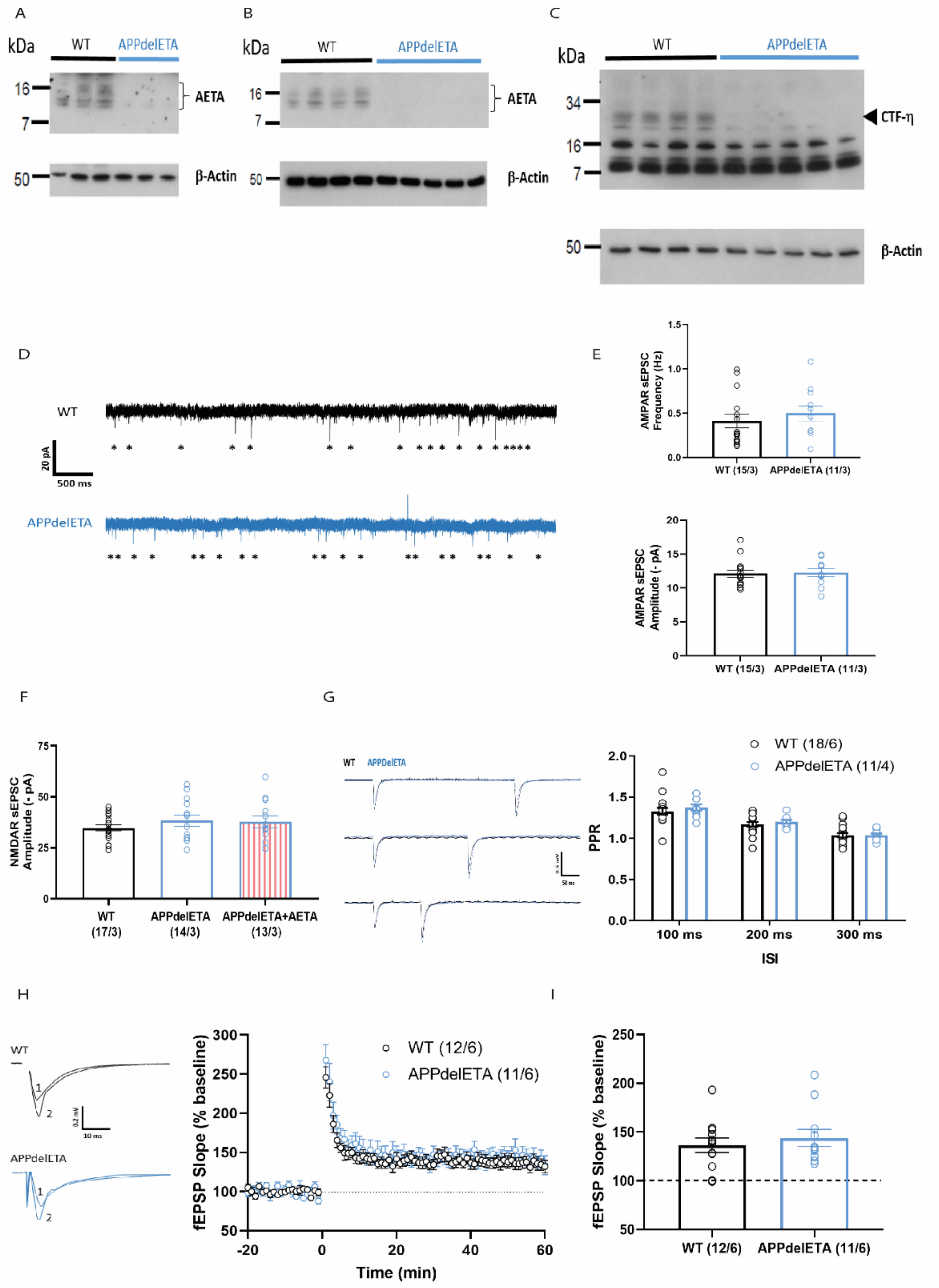
A
kDa
WT
APPdelETA
16
7
AETA
50
β-Actin
B
kDa
WT
APPdelETA
16
7
AETA
50
β-Actin
C
kDa
WT
APPdelETA
34
16
7
CTF-η
50
β-Actin
D
WT
20 pA
500 ms
APPdelETA
E
AMPAR sEPSC Frequency (Hz)
1.5
1.0
0.5
0.0
WT (15/3)
APPdelETA (11/3)
AMPAR sEPSC Amplitude (- pA)
20
15
10
5
0
WT (15/3)
APPdelETA (11/3)
F
NMDAR sEPSC Amplitude (- pA)
75
50
25
0
WT (17/3)
APPdelETA (14/3)
APPdelETA+AETA (13/3)
G
WT
APPdelETA
0.2 mV
50 ms
WT (18/6)
APPdelETA (11/4)
PPR
2.0
1.5
1.0
0.5
0.0
100 ms
200 ms
300 ms
ISI
H
WT
1
2
0.2 mV
10 ms
APPdelETA
1
2
fEPSP Slope (% baseline)
300
250
200
150
100
50
-20
0
20
40
60
Time (min)
WT (12/6)
APPdelETA (11/6)
I
fEPSP Slope (% baseline)
250
200
150
100
50
WT (12/6)
APPdelETA (11/6)

Figure S10 (related to Figure 4) - Blots used for quantification of AETA and CTF-η in WT and APPdelETA hippocampi and measures of AMPAR sEPSC, NMDAR sEPSC amplitude, paired pulse ratios (PPR) and LTP in APPdelETA mice.

(A-B) Two immunoblots for analysis of AETA and β-actin (loading control) levels in DEA samples. AETA level was normalized to β-actin level and then normalized to average WT level for each immunoblot. **(C)** Immunoblot for analysis of CTF-η and β-actin (loading control) levels in RIPA samples. CTF-η level was normalized to β-actin level and then normalized to average WT level. Full blots for (A-C) are provided in additional supplementary material (Data S2). **(D)** Representative traces of AMPAR sEPSC recorded in WT (top) or APPdelETA (bottom) CA1 pyramidal neurons. **(E)** AMPAR sEPSC frequency (top graph) and amplitude (bottom graph calculated from traces as shown in (D). **(F)** NMDAR sEPSC amplitude is normal in APPdelETA mice and not modulated by application of synthetic AETA (10 nM) **(G)** Example traces and PPR measured at three interstimulus intervals (ISI; 100, 200 and 200 ms) at CA3-CA1 synapse in hippocampal slices of WT and APPdelETA mice. **(H)** Example traces and summary graph of fEPSP slope (% baseline) pre- and post-LTP induction (2x 100Hz/1s at 20 s inter-stimulus interval; time 0) at CA3-CA1 synapse in hippocampal slices of WT and APPdelETA mice. **(I)** Bar graph of fEPSP magnitude 45-60 min after LTP induction as fEPSP (% baseline) for data shown in (H). n/N= neurons/mice for E-F; n/N= slices/mice for G-I. See supplemental statistics (*Data S1*) for full statistics.

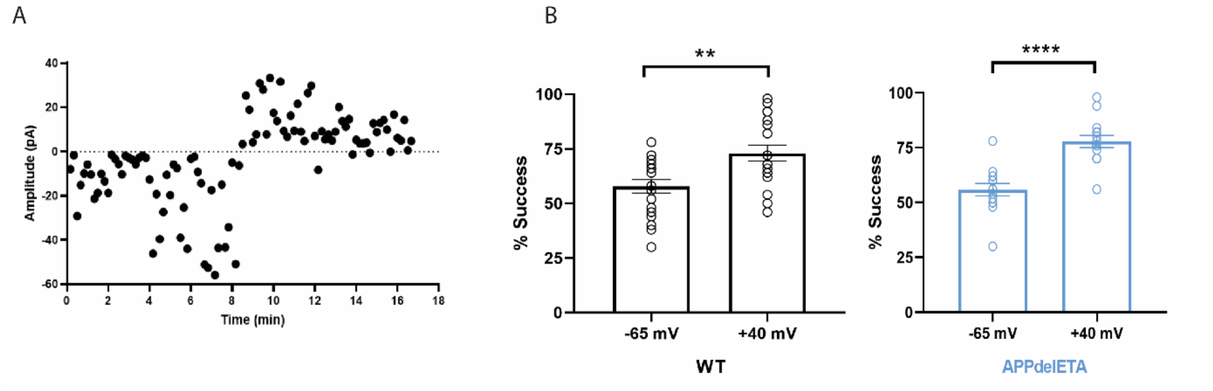

Figure S11 (related to Figure 4) : Absence of η-secretase processing of APP leads to an increase in the number of NMDAR-only containing synapses (silent synapses) in CA1 pyramidal neurons.
(A) Example of a minimal stimulation experiment showing decrease in failures when recording EPSCs at +40 mV versus −65 mV because of activation of silent synapses at +40 mV. **(B)** Average percent success rate when recording at −65 mV versus +40 mV in WT (n/N = 19/3; left panel) and APPdelETA (n/N (neurons/mice) = 14/3; right panel) neurons. See supplemental statistics (*Data S1*) for full statistics.

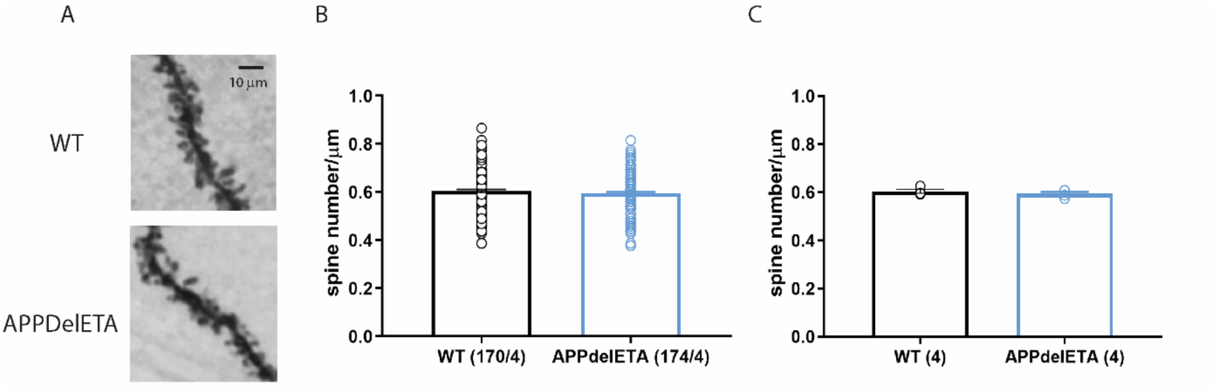

Figure S12 (related to Figure 4) : Absence of η-secretase processing of APP does not perturb the number of spines in the stratum radiatum of CA1 pyramidal neurons.

(A) Example images of segments of dendrites stained by Golgi-Cox and used for analysis of spine density. **(B)** The number of spines per micron was counted in segments from dendrites present in the stratum radiatum of CA1 pyramidal neurons from WT and APPdelETA mice (170 and 174 segments, respectively). **(C)** Same data as in (B) but averaged per mouse (4 mice per genotype). See supplemental statistics (*Data S1*) for full statistics.

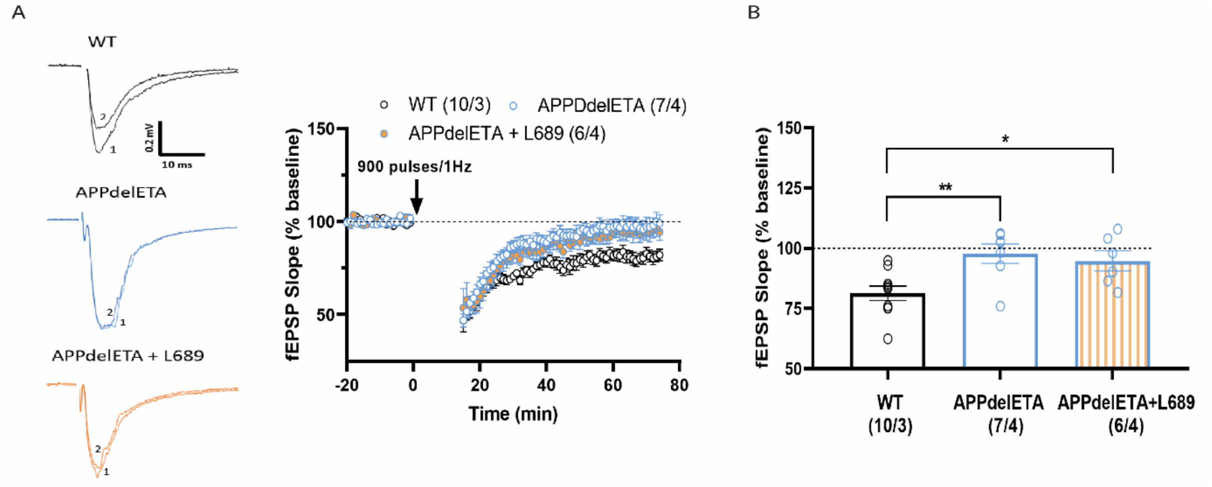

Figure S13 (related to Figure 4) : L689,560 (L689), a potent antagonist of the glycine/D-serine site of NMDARs, does not rescue LTD in APPdelETA mice. (A) Representative traces (left, 1 shows trace pre, 2 shows trace post-induction; scale bars: 10 ms / 0,2 mV) and summary graph (right) of fEPSP slope (% baseline) pre- and post-LTD induction (900 pulses at 1 Hz, time 0) at CA3-CA1 synapse in hippocampal slices of WT and APPdelETA mice without or with supplementation of 10 µM L689 (in recording bath). **(B)** Bar graph of fEPSP magnitude 45-60 min after LTD induction as fEPSP (% baseline) for data shown in (A). n/N= slices/mice. See supplemental statistics (*Data S1*) for full statistics.

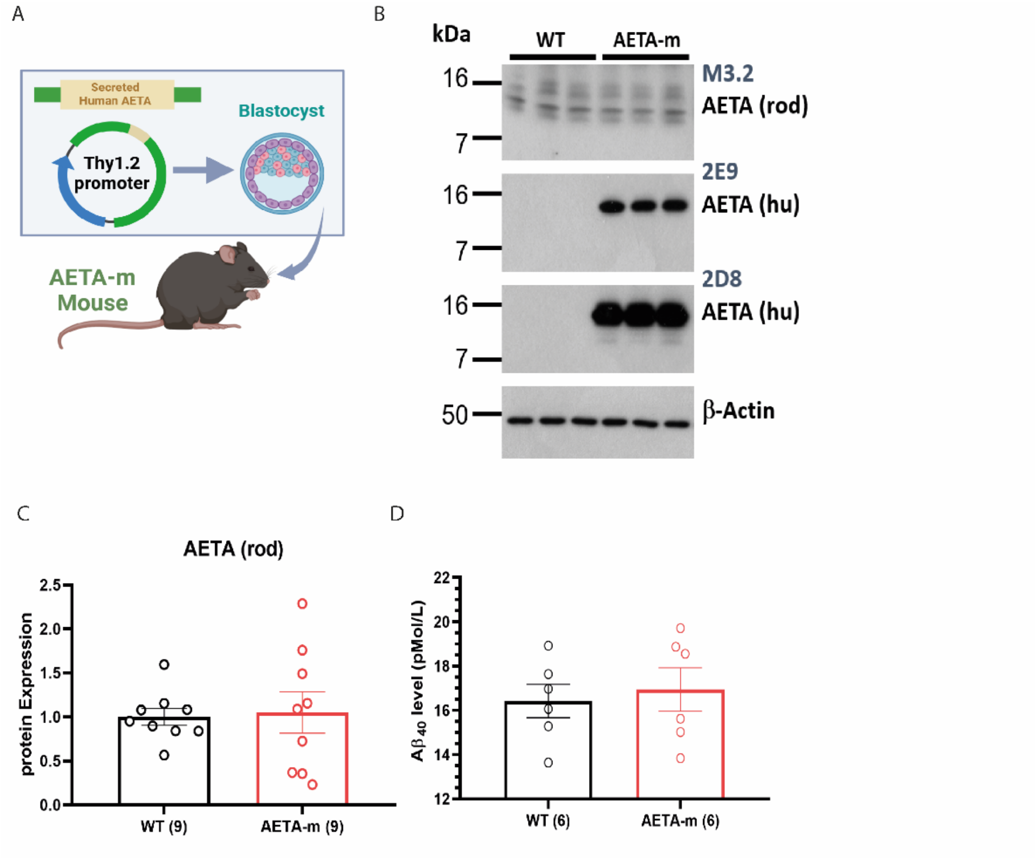

Figure S14 (related to Figure 4) - characterization of AETA-m mouse overexpressing secreted human AETA in the brain. (A) Diagram of production of AETA-m line. **(B)** Example of immunoblot to detect endogenous AETA (rodent (rod); M3.2 antibody) and recombinant secreted human (hu) AETA (long AETA-alpha form) (2D8 and 2E9 antibodies) and β-actin in brains. Full blots are provided in additional supplementary material (Data S2). **(C)** Quantification of endogenous rodent AETA in brain by immunoblotting. **(D)** Quantification of Aβ40 in brain by ELISA. See supplemental statistics (*Data S1*) for full statistics.

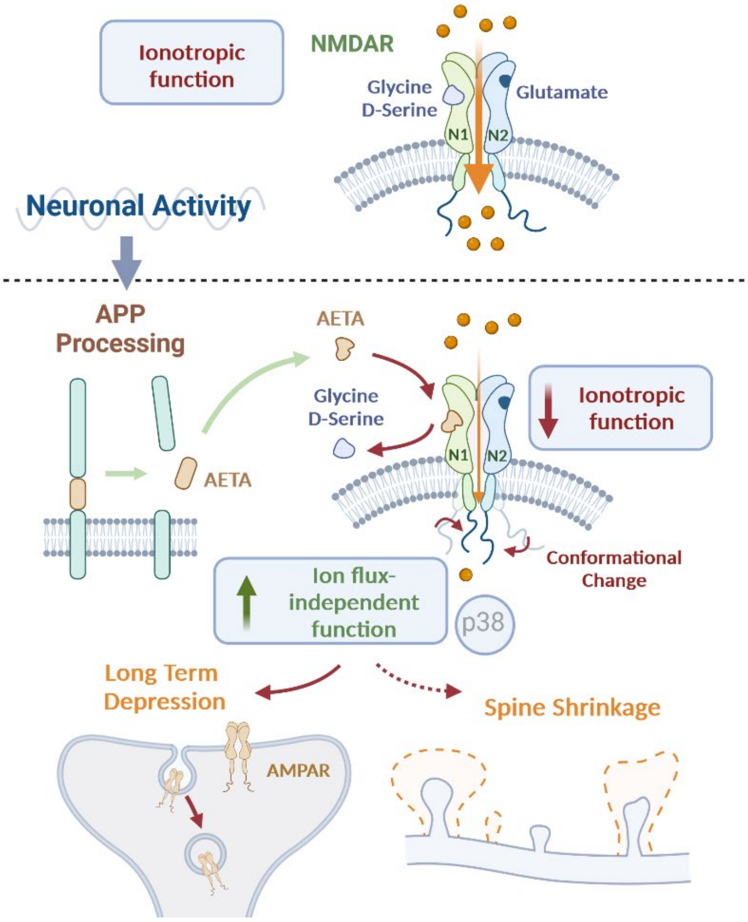

Figure S15 – Summary diagram of AETA-dependent NMDAR activation (ADNA) mechanism. AETA, which is produced by increased neuronal activity, competes with D-serine/Glycine to inhibit NMDAR ionotropic activity. AETA binding leads to a conformational change of NMDARs. AETA also increases p38 phosphorylation. AETA-dependent modulation of NMDARs induces long-term depression (LTD), a NMDAR function that is independent of ion flux. AETA also favors spine shrinkage, in conditions identical to spine shrinkage driven by ion flux-independent and p38-dependent NMDAR signaling. Diagram created by Biorender.com.